Article

Immunity

Expression of the membrane tetraspanin claudin 18 on cancer cells promotes T lymphocyte infiltration and antitumor immunity in pancreatic cancer

Graphical abstract

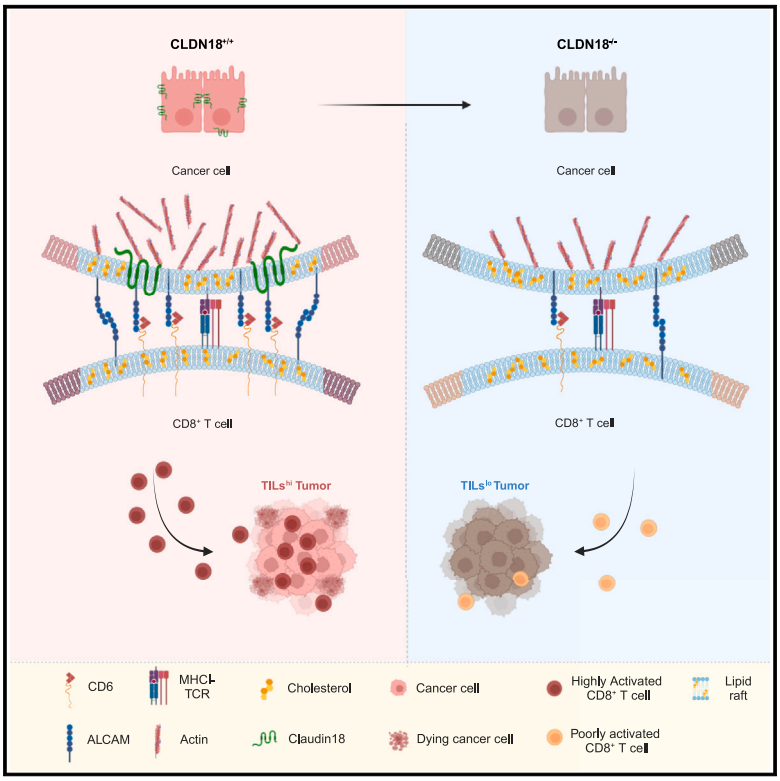

Authors

Francesco De Sanctis, Silvia Dusi, Simone Caligola, ..., Ugur Sahin, Özlem Türeci, Vincenzo Bronte

Correspondence

francesco.desanctis@univr.it (F.D.S.), vincenzo.bronte@iov.veneto.it (V.B.)

In brief

De Sanctis et al. examine the malignancy-associated programs regulating T cell infiltration and function in the tumor environment and find that the tetraspanin claudin 18 on the cancer cell membrane strengthens interaction with T cells, promoting activation, and accrual of tumor-specific lymphocytes and thereby improving antitumor immunity in pancreatic and lung adenocarcinoma.

Highlights

- CLDN18 outlines the subtype and prognosis in pancreatic and lung adenocarcinomas
- CLDN18 sustains CTL infiltration and immune-mediated control of cancer progression
- CLDN18 drives ALCAM to lipid rafts, fueling cell-cell interactions and CTL activation

De Sanctis et al., 2024, Immunity 57, 1378–1393
June 11, 2024
https://doi.org/10.1016/j.immuni.2024.04.021

CellPress

CellPress
OPEN ACCESS

Immunity

Article

Expression of the membrane tetraspanin claudin 18 on cancer cells promotes T lymphocyte infiltration and antitumor immunity in pancreatic cancer

Francesco De Sanctis,[1,17,*] Silvia Dusi,[2,17] Simone Caligola,[2] Cristina Anselmi,[1] Varvara Petrova,[1] Barbara Rossi,[3] Gabriele Angelini,[3] Michael Erdeljan,[4] Stefan Wöll,[4] Anna Melissa Schlitter,[4,5] Thomas Metzler,[6] Katja Steiger,[6] Zea Borok,[7] Peter Bailey,[8] Aline Bauer,[9] Cornelia Halin,[9] Federico Boschi,[10] Rosalba Giugno,[11] Stefania Canè,[2] Rita Lawlor,[10,12] Vincenzo Corbo,[10,12] Aldo Scarpa,[12,13] Gabriela Constantin,[3,14] Stefano Ugel,[1] Fulvia Vascotto,[15] Ugur Sahin,[4,16] Özlem Türeci,[4,16] and Vincenzo Bronte[2,18,*]

[1]Section of Immunology, Department of Medicine, University of Verona, Verona, Italy
[2]Veneto Institute of Oncology IOV-IRCCS, Padua, Italy
[3]Section of General Pathology, Department of Medicine, University of Verona, Verona, Italy
[4]Biopharmaceutical New Technologies (BioNTech) Corporation, Mainz, Germany
[5]Institute of Pathology, School of Medicine, TUM, Munich, Germany
[6]Comparative Experimental Pathology (CEP), Institute of Pathology, School of Medicine, Technical University of Munich, Munich, Germany
[7]Department of Medicine, University of California, San Diego, San Diego, CA, USA
[8]Wolfson Wohl Cancer Research Centre, Institute of Cancer Sciences, University of Glasgow, Garscube Estate, Glasgow, Scotland
[9]Institute of Pharmaceutical Sciences, ETH Zurich, Zurich, Switzerland
[10]Department of Engineering for Innovation Medicine, University of Verona, Verona, Italy
[11]Department of Computer Science, University of Verona, Verona, Italy
[12]ARC-Net Centre for Applied Research on Cancer, University and Hospital Trust of Verona, Verona, Italy
[13]Department of Diagnostics and Public Health, Section of Pathology, University of Verona, Verona, Italy
[14]The Center for Biomedical Computing (CBMC), University of Verona, Verona, Italy
[15]TRON-Translational Oncology at the University Medical Centre of the Johannes Gutenberg University, Mainz, Germany
[16]University Medical Center of the Johannes Gutenberg University Mainz, Mainz, Germany
[17]These authors contributed equally
[18]Lead contact
*Correspondence: francesco.desanctis@univr.it (F.D.S.), vincenzo.bronte@iov.veneto.it (V.B.)
https://doi.org/10.1016/j.immuni.2024.04.021

SUMMARY

Tumors weakly infiltrated by T lymphocytes poorly respond to immunotherapy. We aimed to unveil malignancy-associated programs regulating T cell entrance, arrest, and activation in the tumor environment. Differential expression of cell adhesion and tissue architecture programs, particularly the presence of the membrane tetraspanin claudin (CLDN)18 as a signature gene, demarcated immune-infiltrated from immune-depleted mouse pancreatic tumors. In human pancreatic ductal adenocarcinoma (PDAC) and non-small cell lung cancer, CLDN18 expression positively correlated with more differentiated histology and favorable prognosis. CLDN18 on the cell surface promoted accrual of cytotoxic T lymphocytes (CTLs), facilitating direct CTL contacts with tumor cells by driving the mobilization of the adhesion protein ALCAM to the lipid rafts of the tumor cell membrane through actin. This process favored the formation of robust immunological synapses (ISs) between CTLs and CLDN18-positive cancer cells, resulting in increased T cell activation. Our data reveal an immune role for CLDN18 in orchestrating T cell infiltration and shaping the tumor immune contexture.

INTRODUCTION

While effective across a range of different cancers, immune checkpoint inhibitors fail to induce significant therapeutic responses in tumors with a low mutational tumor burden[1–3] and sparse immune cell and T cell infiltration.[4,5] Such cancers are referred to as poorly infiltrated tumors, with pancreatic ductal adenocarcinoma (PDAC) being a paradigmatic example.[6] The 5-year survival rate of PDAC is well below 10%, and PDAC is predicted to rise to the second leading death cause for cancer by 2030.[7] PDAC is usually diagnosed in an advanced stage; thus, only 15%–20% of patients can benefit from curative surgery. For the vast majority, palliative chemotherapy, to which PDAC is not particularly sensitive, remains the last treatment option.

The determinants associated with the poorly infiltrated tumor landscape and failure of immune checkpoint inhibitors in PDAC are still not fully understood. Pancreatic cancer cells cooperate with immunoregulatory cells, endothelial cells, and fibroblasts to establish a hostile immunosuppressive tumor microenvironment (TME)[8] associated with ineffective priming of tumor-specific adaptive immune responses[9] and the poor amount and fitness of tumor-infiltrating lymphocytes (TILs).[10,11] The common view that PDAC is an immune desert has been recently reconsidered due to novel insights. First, current evidence suggests that the TME can be manipulated to restore efficient antigen presentation[12] and myeloid function can be remodeled toward an antitumor phenotype,[13] laying the ground for effective chemo-immunotherapy.[14] Second, new molecular classifications, including clinicopathological features, allow the definition of distinct PDAC subtypes. These molecular signatures improve the classification of tumor histopathological features and can better predict the outcome and response to therapy in PDAC patients.[15–17] Established molecular classifications share peculiar signatures associated with adenosquamous carcinoma, named quasimesenchymal (QM),[15] basal like,[16] and squamous[17] subtypes, which are commonly associated with worse overall survival (OS). Other signatures are associated with more differentiated and epithelial cell phenotype, named classical,[15,16] which divides into pancreatic progenitor, immunogenic, and aberrantly differentiated endocrine exocrine (ADEX),[17] characterized by brisk immune infiltrates and better OS.

Claudins (CLDNs) are a family of 27 membrane tetraspanins involved in the establishment of tight junctions, paracellular barriers with distinct features, and in maintaining the architecture and biological functions of tissues in many organs.[18] CLDN18 has two splice variants that are strictly cell lineage dependent. Variant 1 (CLDN18.1) is exclusive in normal lung tissue and deranged in lung cancer. Variant 2 (CLDN18.2) expressed on gastric epithelial cells regulates the stomach paracellular barrier, providing resistance to H^+ leakage, and its downregulation supports inflammation.[19,20] CLDN18.2 escapes strict transcriptional control during tumorigenesis and is ectopically expressed in various tumor types, such as human preneoplastic pancreatic lesions (pancreatic intraepithelial neoplasias [PanINs]) and PDACs.[21] Due to its cancer-selective expression, CLDN18.2 is an attractive therapeutic target. Recently, 2 phase 3 trials showed that Zolbetuximab, an IgG1 antibody directed against CLDN18.2, resulted in survival benefit of patients with advanced gastric cancer (identifier: NCT03504397).[22] The same antibody is currently tested in a randomized phase 2 study in pancreatic cancer (identifier: NCT03816163). Chimeric antigen receptor (CAR) T cells directed against CLDN18.2 are in preclinical and clinical development for adoptive cell transfer (ACT, NCT04404595).[23,24]

Here, we sought to investigate the strategies engaged by immunotherapy-resistant solid tumors. Employing mouse pancreatic tumor models categorized as either highly or poorly permeated by TILs, we unveiled neoplastic programs leading to T lymphocyte entrance and interaction with tumor cells. In particular, we defined a role for CLDN18 in regulating host cancer immunity. We found that CLDN18 expression supported T lymphocyte infiltration and survival in both pancreatic and lung cancer. Mechanistically, CLDN18 strengthened the contacts between T lymphocytes and tumor cells, leading to the formation of the immunological synapse (IS), T cell activation, cytotoxicity, and cytokine release through activated leukocyte cell adhesion molecule (ALCAM) accrual to the tumor cell membrane, and consequent homotypic (ALCAM-ALCAM) and heterotypic (ALCAM-CD6) interactions with cytotoxic T lymphocytes (CTLs).

RESULTS

Characterization of mouse models for "TILs^{hi}" and "TILs^{lo}" pancreatic tumors

To investigate cancer cell factors promoting either a TILs^{hi} or TILs^{lo} TME in pancreatic cancer, we used a Kras$^{LSL\text{-}G12D/+}$, Trp53$^{LSL\text{-}R172H/+}$, Pdx1-Cre (KPC) PDAC mouse model.[25] Four KPC cell lines were developed that either expressed only the endogenous telomerase (TERT) tumor-associated antigen (TAA) (FC1199 and FC1242 cell lines) or were engineered to produce ovalbumin (OVA) as strong surrogate tumor antigen (hereafter referred to as FC1199-OVA and FC1242-OVA cells). The established cell lines were characterized for MHCI and OVA expression (Figures S1A and S1B) and recognition and killing by either OVA-specific (Figure S1C, left) or TERT-specific CTLs (Figure S1C, right). While no relevant differences were observed *in vitro*, only the growth of FC1199-OVA was completely inhibited in immunocompetent C57BL/6 mice, regardless of whether it was injected subcutaneously (Figure 1A), intravenously (i.v.) to induce lung metastases (Figures S1D and S1E), or orthotopically into the pancreas (Figures S1F–S1I). Host immunocompetence was mandatory for effective control of FC1199-OVA, as antitumor activity was completely abrogated in immunocompromised Rag2$^{-/-}$ (B10;B6-*Rag2*^{tm1Fwa} *Il2rg*^{tm1Wjl}) mice lacking adaptive immunity (Figures S1E, S1H, and S1I). However, the antitumor activity against FC1199-OVA was not based on a superior T cell immune response toward the OVA antigen. In fact, both FC1242-OVA and FC1199-OVA cells elicited comparable levels of OVA-specific CTLs, as confirmed by interferon (IFN)-γ spot counts in splenocytes of C57BL/6 tumor-bearing mice (Figures S1J and S1K). We investigated whether the increased tumor control in FC1199-OVA-bearing mice could be due to differential homing of T cells to the tumor. As a source of OVA-specific CTLs, we cultured total OT-I splenocytes with SIINFEKL peptide and interleukin (IL)-2 for 3 days, and after 1 day of resting we transferred them to tumor-bearing mice. The ACT of tumor-specific CTLs was completely ineffective in FC1242-OVA-bearing immunodeficient mice but successfully curbed tumor growth and improved survival of FC1199-OVA-bearing immunodeficient mice (Figures 1B and S2A). 3 days after ACT, we detected more CTLs in FC1199-OVA than in FC1242-OVA tumors by flow cytometry (FC) (Figures 1C right, S2B, and S2C) and immunohistochemistry (IHC) (Figure 1D), but not in peripheral immune organs such as the spleen (Figure 1C, left).

Principal-component analysis (PCA) revealed different molecular signatures in the two KPC-derived cell lines (Figure S2D). We compared these signatures with gene expression profiles in the molecular classification system that is based on correlating histological features of human PDACs with OS.[17] To accomplish this task, we used gene set variation analysis (GSVA[27]), which assigns for each gene set signature an enrichment score to each RNA sequencing (RNA-seq) sample. FC1242-OVA

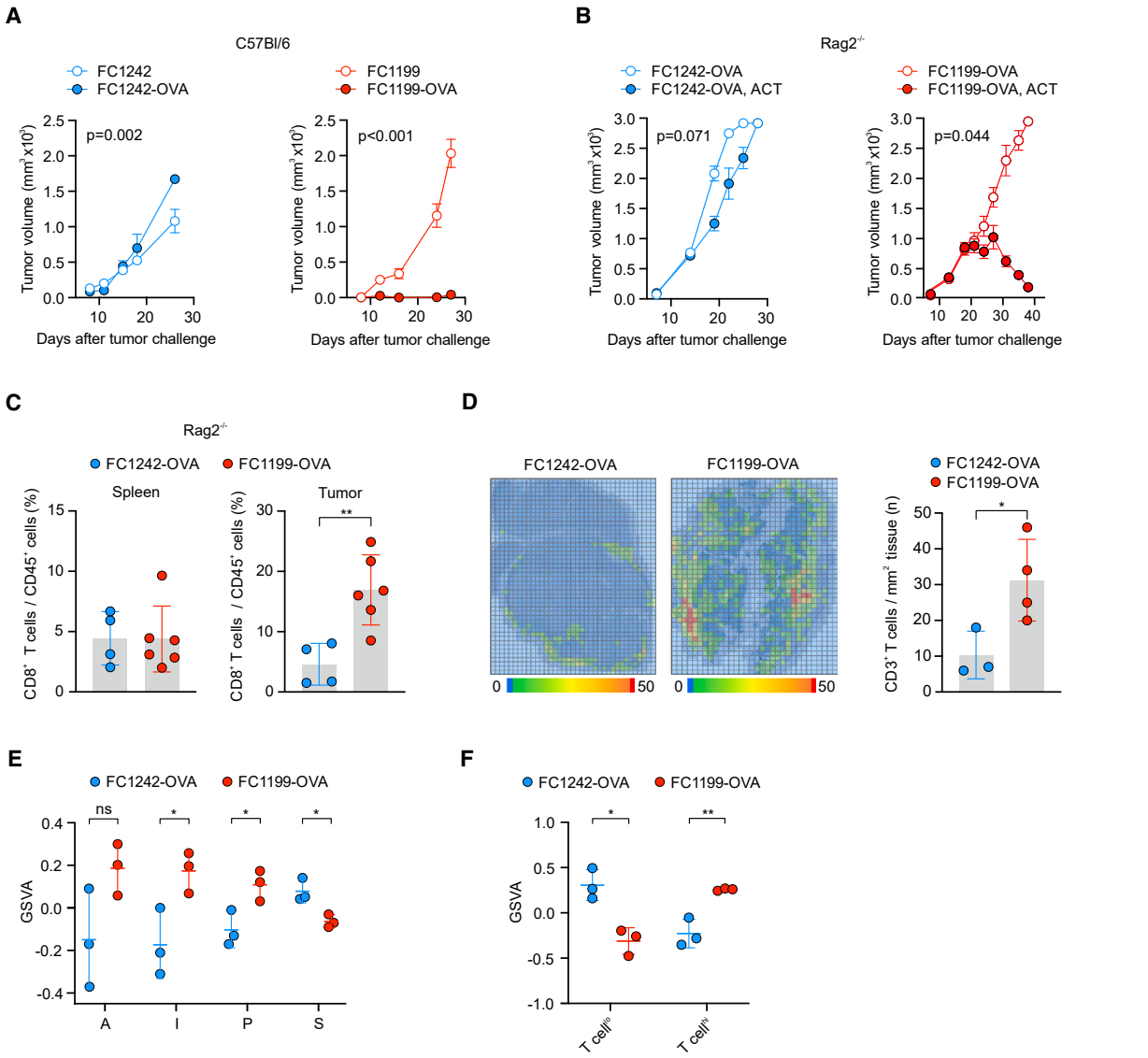

Figure 1. FC1242-OVA and FC1199-OVA recapitulate TILs^{lo} and TILs^{hi} pancreatic adenocarcinoma tumors

(A) Tumor growth curves of immunocompetent mice (C57BL/6) bearing FC1242, FC1242-OVA, FC1199, and FC1199-OVA, s.c. tumors (n = 5/group).

(B) Tumor growth curves of immunodeficient mice (Rag2$^{-/-}$) bearing either FC1242-OVA or FC1199-OVA s.c. tumors, treated or not with adoptive cell transfer (ACT) of OVA-specific CTLs. Data are presented as mean ± SEM. Two-way ANOVA (A and B).

(C) Flow cytometry (FC) frequency quantification of CD8$^+$ T cells in spleen (left) and in tumors (right) of Rag2$^{-/-}$ mice treated as in (B) and euthanized 3 days after ACT to quantify OVA-specific CTLs. $^{**}p$ = 0.005.

(D) Representative immunohistochemistry (IHC) heatmap plot images (left) and CD3$^+$ T cell in tumor tissue (right) of Rag2$^{-/-}$ mice treated as in (B) and euthanized 3 days after ACT. Data are presented as mean ± SD. Unpaired, two-tailed t test (C and D). $^{*}p$ = 0.038.

(E) Gene set variation analysis (GSVA) scores of FC1242-OVA and FC1199-OVA on PDAC molecular classifications[17] (A, ADEX; I, immunogenic; P, progenitor; S, squamous).

(F) GSVA scores of FC1242-OVA and FC1199-OVA on the gene signatures of KPC-derived cell lines characterized as TILs^{hi} and TILs^{low}.[26] Unpaired, two-tailed t test (E and F). *p < 0.05; **p = 0.009.

resembled the "squamous" cell tumor subtype that is associated with poor prognosis. Conversely, FC1199-OVA showed a "classical subtype" signature shared with ADEX, progenitor, and immunogenic PDACs (Figure 1E).

We then compared the molecular profiles of both cell lines with the signatures of a panel of mouse PDAC lines classified as TILs^{lo} or TILs^{hi} based on the low and high numbers of TILs in the TME.[26] GSVA computed on FC1242-OVA and FC1199-OVA employing both TILs^{hi} TILs^{lo} signatures[26] (Figure 1F) and molecular subtype classifications[17] (Figure S2E) indicated that the molecular signature of FC1199-OVA was similar to TILs^{hi} cell lines, while FC1242-OVA resembled TILs^{lo}.

Altogether, these data indicated that failure of growth control of FC1242-OVA by adaptive immunity correlated with a deficit

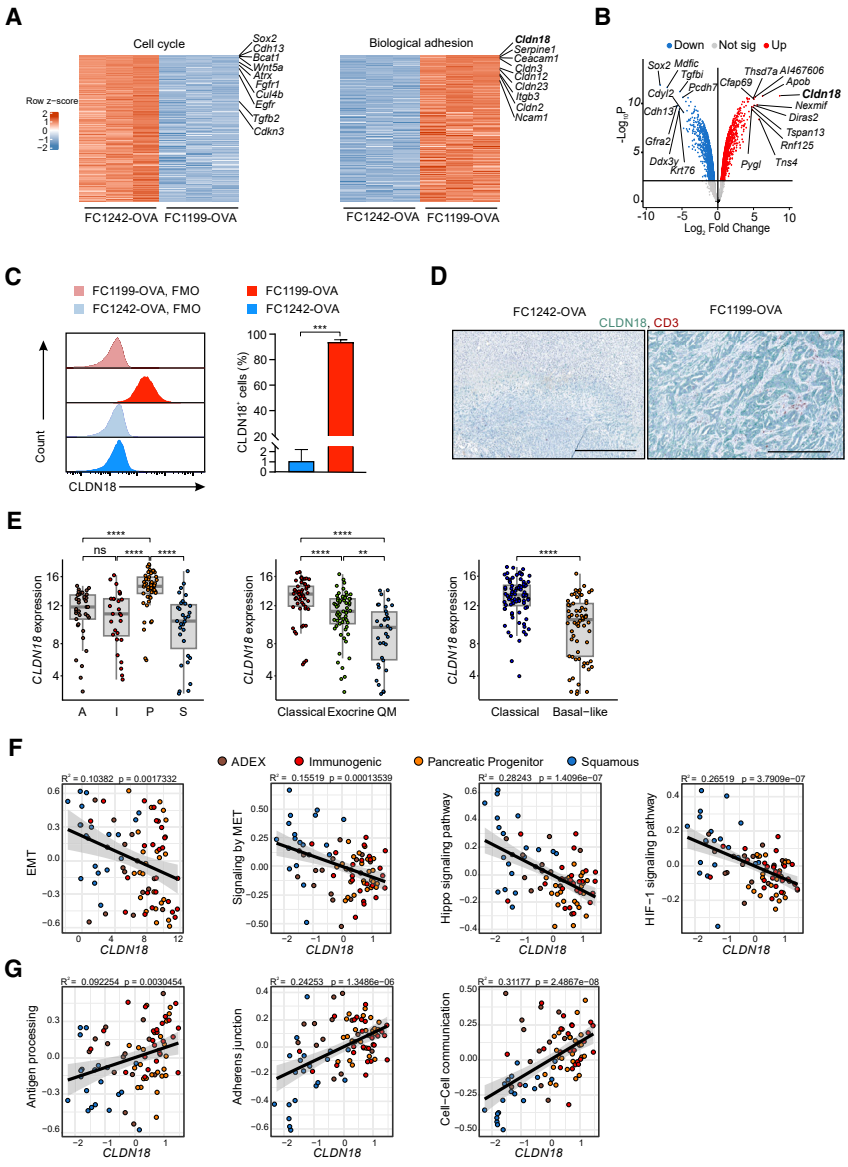

Figure 2. FC1199-OVA TILs^{hi} tumor cell line presents a molecular signature associated with biological adhesion processes and CLDNs expression

(A) Heatmap of genes involved in cell cycle (FC1242-OVA) and biological adhesion (FC1199-OVA) processes (Gene Ontology).

(B) Volcano plot of differentially expressed genes in FC1199-OVA cell line compared with FC1242-OVA cell line. Top upregulated (red) and downregulated (cyan) genes are shown.

(C) Representative fluorescence-activated cell sorting (FACS) histogram plots and frequency of FC1199-OVA and FC1242-OVA cells expressing CLDN18 protein. Data are presented as mean ± SD. Unpaired, two-tailed t test. ***$p < 0.001$.

(D) Representative IHC images of tumor tissues derived from FC1199-OVA and FC1242-OVA cell lines injected s.c. in immunodeficient mice treated with ACT. CLDN18 (green) and CD3 (red); scale bars, 500 μm.

(E) *CLDN18* expression on TCGA PAAD dataset annotated with the molecular classifications according to Bailey et al.[17] (left), Collisson et al.[15] (central), and Moffitt et al.[16] (right). Dunn test. **$p < 0.01$; ****$p < 0.0001$.

(F and G) Linear associations between *CLDN18* and epithelial to mesenchymal transition (EMT), signaling by MET, Hippo and HIF-1 pathways, antigen processing, adherents junction, and cell-cell communication. The goodness of fit (R^2) and the *p* value of the linear association are reported.

in T cell homing to the tumor resulting in a lack of T cell infiltrates and that, by virtue of their biological asset and molecular profile, FC1199-OVA and FC1242-OVA tumors qualified as models for TILs^{hi} and TILs^{lo} PDACs, respectively.

Cell adhesion signature and CLDN18 expression correlate with T cell infiltration and an immunogenic tumor contexture

We characterized PDAC tumors derived from both cell lines to identify gene candidates for the differences in T cell infiltration. Gene ontology analysis revealed a signature in the FC1242-OVA (TILs^{lo}) that was associated with biological processes related to cell proliferation, cell division, DNA replication, and DNA nuclear organization (Figure S2F). Genes such as *Sox2*, *Bcat1*, *Fgfr1*, *Egfr*, and *Tgfb2* related to stemness[28] resistance to chemotherapy,[29] immunosuppression, and tumor progression[30,31] were upregulated (Figure 2A left).

In contrast, the FC1199-OVA (TILs^{hi}) cell line had a unique signature associated with biological processes related to cell surface receptor signaling, cell adhesion, cytokine production, and regulation of immune processes. We identified several membrane proteins associated with cell anchorage and adherent junctions within the cellular components (Figure S2G). Among the overexpressed biological adhesion process genes in FC1199-OVA tumor, we found several receptors with cell-cell interaction properties, including adhesion molecules, integrins, and a family of proteins involved in tight junction formation and maintenance, i.e., CLDNs (Figure 2A right), with CLDN18 being the most upregulated (Figures 2A right and 2B; Table S1). By FC and IHC, we confirmed that CLDN18 was strongly expressed in FC1199-OVA but not FC1242-OVA mouse tumors (Figures 2C and 2D).

By comparing PDAC molecular classifications[15–17] within The Cancer Genome Atlas (TCGA) pancreatic adenocarcinoma dataset (PAAD),[32] we also noticed CLDN18 association with classical, progenitor (P), ADEX (A), and immunogenic (I) PDAC subtypes (Figure 2E). By interrogating the International Cancer Genome Consortium (ICGC) molecular dataset,[17] we identified a significant inverse correlation between CLDN18 and molecular programs for processes associated with neoplastic progression, including epithelial to mesenchymal transition (EMT) and signaling pathways of c-MET, Hippo, and hypoxia-inducible

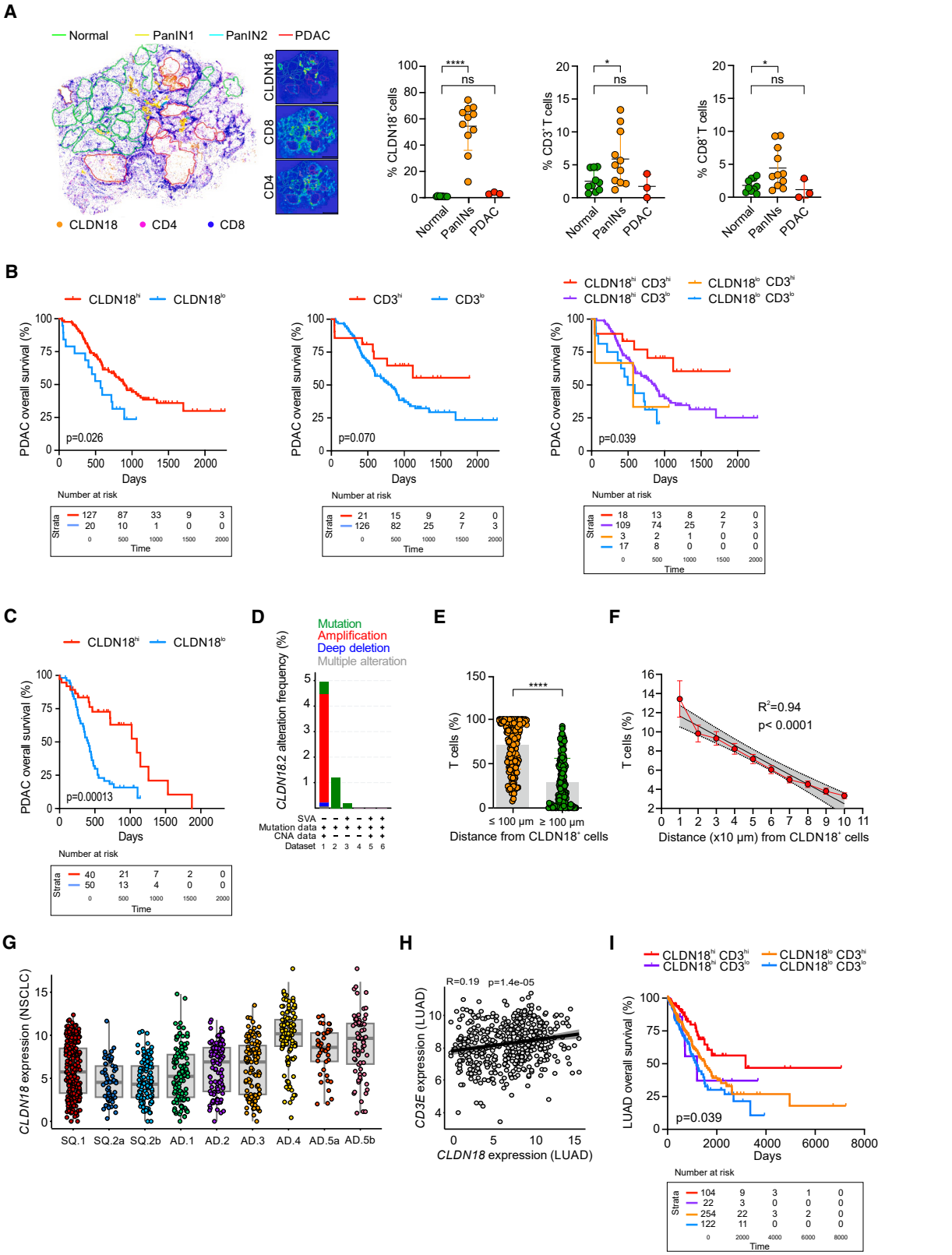

(legend on next page)

factor 1 (HIF-1) (Figure 2F). On the contrary, we unveiled a positive correlation between CLDN18 expression and programs regulating tissue architecture, cell-cell communication, and immune activation (Figure 2G).

Altogether, these data indicated that molecular programs related to cell adhesion and tissue architecture, with CLDN18 as the main signature gene, differentiated FC1199-OVA (TILs^{hi}) from FC1242-OVA (TILs^{lo}) tumors. In human PDAC, CLDN18 expression correlated with a more differentiated histology and immunogenicity markers that are all linked to a more favorable prognosis.

CLDN18 is a prognostic biomarker for the OS of PDAC patients

We examined primary tumor tissues from a cohort of patients with early-stage pancreatic cancer. CLDN18, CD4, and CD8 multiple IF images were overlaid with hematoxylin and eosin (H&E) staining to integrate pathological information. Different tissue regions were classified by a pathologist as normal, early-stage neoplasia called PanIN, or PDAC (Figure 3A left). CLDN18, absent in normal pancreatic tissue, was highly expressed on epithelial cells of PanIN stages and, at lower levels, in PDAC (Figure 3A right). CD3$^+$ and CD8$^+$ T lymphocyte presence similarly trended, with brisk infiltration in PanINs and exclusion in PDAC (Figure 3A right). Then, we performed a dual IHC for CLDN18 and CD3 in microarray tissue samples from 148 PDAC patients (Table 1) to evaluate the prognostic role of CLDN18 in PDAC. The analysis revealed that CLDN18 alone had a higher prognostic value than TILs for favorable OS (Figure 3B). This result was confirmed also by multivariable Cox analysis adjusting for the following risk factors: age, gender, residual tumor, and stage (Table S2). Similar results were obtained for disease-free survival (DFS; Figure S3A).

The presence of TILs together with CLDN18 further stratified patients with improved clinical performance (Figures 3B and S3A). We confirmed the relevance of these findings in independent cohorts of PDAC patients by interrogating the ICGC dataset[17] (Figure 3C; Table S3). Notably, genome sequencing confirmed that CLDN18 downregulation in PDAC was the consequence of transcriptional regulation rather than genetic mutations of the *CLDN18* gene as supported by genome sequencing (Figure 3D). In addition, by tracking TIL localization in microarray tissues of CLDN18-positive PDAC cases, we found that CD3$^+$ T lymphocytes were preferentially located near CLDN18$^+$ tumor cells (Figure 3E), as also proved by the inverse correlation between TILs and the distance from CLDN18$^+$ cells (Figure 3F).

We wondered whether the correlation of CLDN18 with molecular subtype, immune contexture, and clinical outcomes was tissue type specific. To this end, we examined the available TCGA datasets of human non-small cell lung cancer (NSCLC) with the molecular classification established for this tumor type.[33] The *CLDN18.1* variant is often deregulated in lung cancer. We revealed the preferential *CLDN18* expression in adenocarcinomas of the lung adenocarcinoma (LUAD) over squamous cell carcinomas (Figure 3G). *CLDN18* expression was particularly high in AD.4 and AD.5 subtypes of LUAD, both of which are associated with high immune cell infiltration and better survival.[33] Further, we identified a significant positive correlation between *CLDN18* expression and immune infiltration with *CD3E* T lymphocytes (Figure 3H) in LUAD patients. CLDN18 expression in conjunction with the presence of TILs (as either CD3 or CD8) within the tumor of LUAD patients was associated with improved OS (Figures 3I and S3B; Table S4).

Altogether, CLDN18 variants were associated with TILs and represented a stand-alone prognostic biomarker of improved OS in both PDAC and LUAD. Moreover, CLDN18 concurred with TILs to stratify the patients with improved clinical outcomes.

CLDN18 expression drives CTL infiltration in tumor

To prove the CLDN18 involvement in T cell infiltration, we deleted the *Cldn18* gene using CRISPR-Cas9 technology in the FC1199-OVA cell line and generated a series of CLDN18$^{-/-}$ clones, as confirmed by FC (representative clone in Figure S4A) and Sanger sequencing (Figure S4B), while similar levels of OVA protein expression were maintained (Figure S4C).

We injected CLDN18$^{+/+}$ and CLDN18$^{-/-}$ FC1199-OVA clones into immunodeficient Rag2$^{-/-}$ mice. Infiltration of adoptively transferred, OVA-specific CTLs into tumors was significantly impaired in CLDN18$^{-/-}$ FC1199-OVA derived tumors as shown by FC (Figures 4A and S4D) and IHC (Figure 4B). We employed "earthquake" analysis to track the positioning of T cells from the center to the periphery of tumor tissue (Figure S4E) and found that CLDN18 ablation significantly impaired the presence of

Figure 3. CLDN18 is a prognostic biomarker of better OS in PDAC patients

(A) Representative spatial analysis of pancreatic tissues from patients diagnosed with early-stage pancreatic tumors. Different pancreatic areas (normal in green, PanIN1 in yellow, PanIN2 in cyan, and PDAC in red) and cell phenotypes (CLDN18$^+$ tumor cells in orange, CD4$^+$ in pink, and CD8$^+$ T cells in blue) were annotated by the pathologist (left). Scale bar = 5 mm. Frequency of CLDN18$^+$ tumor cells, CD3$^+$ and CD8$^+$ TILs in the different areas of pancreatic tissue (right). Unpaired, two-tailed t test. *$p < 0.05$; ****$p < 0.0001$.

(B) Kaplan-Meier curves showing the overall survival of 148 PDAC patients based on CLDN18 expression and TILs (CD3) from IHC staining as single markers or in association (upper).

(C) Kaplan-Meier curves showing the overall survival of PDAC patients[17] based on *CLDN18* expression (upper).

(D) Genomic analysis performed on available PDAC datasets (cBioPortal for Cancer Genomics—Memorial Sloan Kettering Cancer Center) revealing that *CLDN18.2* is not target of mutation events during cancer progression (dataset: 1_TCGA, Nature 2020; 2_Dana Farber, Nat Genet 2018; 3_Umich, Nature 2017; 4_MSK, 5_Nat Genet 2020; 6_MSK, Clin. Cancer Res. 2020).

(E) Quantification of the number of T cells either close (distance < 100 μm) or far (distance > 100 μm) from CLDN18$^+$ cells within the CLDN18$^+$ PDAC cases. Data are presented as mean ± SD. Mann-Whitney test, two tailed. ****$p = 0.0001$.

(F) T cells distribution in term of percentage at different distances from CLDN18$^+$ tumor cells. Statistic was calculated by the Shapiro Wilk function. Simple linear regression. T cells preferentially localize in proximity of CLDN18$^+$ tumor cells in PDAC microenvironment.

(G) *CLDN18* expression in molecular subtypes of NSCLC.[33]

(H) Scatter plot showing linear association and Spearman's correlation between *CLDN18* expression and *CD3E* in LUAD.

(I) Kaplan-Meier curve showing the overall survival of LUAD patients based on *CLDN18* and *CD3E* expression. Log-rank test (B, C, and I). Table with the number of patients at risk in the panel below.

Table 1. Clinical characteristic of enrolled PDAC patients

Anagraphic	
Male, *n* (%)	84 (56.7)
Female, *n* (%)	64 (43.2)
Age at diagnosis, median (interquartile range [IQR])	59.5 (36–72.9)
Clinical information	–
Grade G1, *n* (%)	8 (5.4)
Grade G2, *n* (%)	92 (62.2)
Grade G3, *n* (%)	48 (32.4)
Stage IIA, *n* (%)	15 (10.1)
Stage IIB, *n* (%)	130 (87.8)
Margin R0, *n* (%)	94 (63.5)
Margin R1, *n* (%)	54 (36.5)
Adjuvant chemotherapy only, *n* (%)	88 (67.7)
Adjuvant radiotherapy only, *n* (%)	2 (1.5)
Adjuvant chemo + radiotherapy, *n* (%)	28 (21.5)
Recurrence, *n* (%)	78 (61.9)

TILs, particularly near the inner tumor core (Figure 4C). T lymphocyte infiltration in CLDN18$^{+/+}$ FC1199-OVA was associated with increased expression of genes related to lymphocyte activation and killing in tumor tissue, including tumor necrosis factor alpha (*Tnf-α*) and granzyme-B (*Gzm-B*) (Figure 4D), indicating the functionality of recruited T cells. Although CLDN18$^{+/+}$ and CLDN18$^{-/-}$ FC1199-OVA tumors grew comparably in untreated mice (Figure S4F), CLDN18$^{+/+}$ tumors were better controlled by OVA-specific CTLs in mice receiving ACT (Figure 4E). Since FC1199-OVA is efficiently lysed by TERT-specific CTLs *in vitro* (Figure S1C), we sought to support further the role of CLDN18 in an orthotopic tumor setting. We orthotopically injected CLDN18$^{+/+}$ and CLDN18$^{-/-}$ FC1199-OVA cells in immunodeficient Rag2$^{-/-}$ mice and, after 2 weeks, we supplied TERT-specific CTLs. Three days following ACT, we identified significantly higher CTLs in CLDN18$^{+/+}$ FC1199-OVA-derived tumors (Figure S4G). Increased CTL infiltration was associated with significant tumor control in CLDN18$^{+/+}$ FC1199-OVA tumors, which was not observed in CLDN18$^{-/-}$ FC1199-OVA tumors (Figure S4H).

We then investigated whether enhanced CLDN18 expression could support the antitumor activity of T lymphocytes in FC1242-OVA (TILs^{lo}) tumors. First, we demonstrated that *in situ* delivery of CLDN18-GFP was efficiently carried by lentiviral transduction (Figure S4I, left). Most of the transduced cells were tumor cells (approximately 70%) and leukocytes (Figure S4I, right). Having demonstrated that this strategy successfully introduced CLDN18 in the tumor environment, we injected *in situ* either GFP-CLDN18 or luciferase lentiviruses (control) in immunodeficient mice bearing FC1242-OVA tumors, followed by ACT 3 days later. Lentivirus infection alone did not confer any benefit compared with control whereas ectopic CLDN18 expression significantly improved ACT efficacy (Figure 4F).

To reassess our findings in a humanized model, we employed human HLA-A2^{+}, CLDN18-negative PDAC cell line and its stably CLDN18.2-transfected counterpart (DANG and DANG-CLDN18, respectively) both endogenously expressing human (h)TERT (Figure S5A). These cells were injected into opposite flanks of immunodeficient, *NOD Cg-Prkdcscid Il2rgtm1Sug/Jic-Tac* (NOG) mice. Once xenograft tumors were established, mice underwent adoptive transfer of TCR-engineered, human T lymphocytes recognizing hTERT with high avidity.[34,35] Again, T lymphocytes were preferentially detected in the CLDN18$^{+/+}$ tumors, as shown by both FC (Figures 4G and S5B) and IHC (Figure 4H); moreover, T cell infiltration was associated with significantly improved control of tumor progression (Figure 4I).

We recapitulated the three-dimensional tumor architecture *in vitro* by establishing T lymphocyte-spheroid co-cultures derived from DANG and DANG-CLDN18 tumors (Figure S5C). The presence of CLDN18 supported T cell adhesion to the tumor spheroids, as shown by T cell quantification (Figure S5D left) and IF imaging (Figure S5D right).

CLDN18 is known to regulate H^{+} fluxes and maintain the acidic pH microenvironment in the stomach, and acidic pH can epigenetically rewire stemness and cytotoxicity of T cells.[36,37] We did not detect a significant difference in pH between DANG and DANG-CLDN18 tumors *in vivo* (Figure S5E). Moreover, we confirmed that CTL recruitment to tumors was not affected by soluble chemoattractants upregulated in a CLDN18-dependent manner. No differences were observed between DANG-CLDN18 and DANG cell conditioned medium in the ability to attract either activated or resting T lymphocytes (Figure S5F).

Finally, we investigated whether loss of CLDN18 lung isoform could impair cancer immune surveillance. As autochthonous CLDN18-proficient and CLDN18-deficient LUAD model,[38] we established, the *LSL-Kras*$^{G12D/+}$ *LSL-Trp53*$^{R172H/+}$ CLDN$^{flox/flox}$ (KPCldn$^{fl/fl}$) mice. In KPCldn$^{+/+}$ and KPCldn$^{fl/fl}$ mice, lung cell infection with a CRE lentivirus drove the activation of oncogenic Kras, Trp53 loss, and eventually CLDN18 deletion in floxed mice. Lungs were freshly isolated, and tumor burden was assessed by blinded veterinary pathologist analysis according to a three-step grading system (grade 1 [G1], well differentiated, low grade; grade 2 [G2], moderately differentiated, intermediate grade; grade 3 [G3], undifferentiated, high grade).[38,39] Reference lung sections from CLDN18$^{+/+}$ and CLDN18$^{-/-}$ mice and the number of lesions classified by stage of progression are shown in Figures 4J and 4K. We identified a higher number of grade 1 and grade 2 tumor foci in CLDN18$^{-/-}$ compared with CLDN18$^{+/+}$ mice (Figure 4K). In accordance, CLDN18 loss was associated with impaired infiltration of CD8 CTLs in both grade 1 and grade 2 lesions (Figures 4L and 4M). These results were confirmed by establishing lung tumor lesions in CLDN18$^{+/+}$ and CLDN18$^{-/-}$ context employing a CRE lentivirus engineered to express firefly luciferase fused with the SIINFEKL peptide (Lenti-lucOS[38]). Lungs were freshly isolated, and tumor burden was assessed by bioluminescence imaging (Figure S5G) and by a blinded pathologist (Figures S5H and S5I). Collectively, results from autochthonous LUAD models suggested that loss of CLDN18 promoted the progression of early cancer lesions.

In summary, these data indicated a direct role of CLDN18 expression in supporting CTL infiltration of the tumor core and promoting cancer immunotherapy.

CLDN18 on cancer cells supports the formation of the IS, tumor-T cell interaction, and T cell activation

We tracked *in vivo* the intra-tumor dynamics of OVA-specific CTLs in CLDN18$^{+/+}$ and CLDN18$^{-/-}$ FC1199-OVA

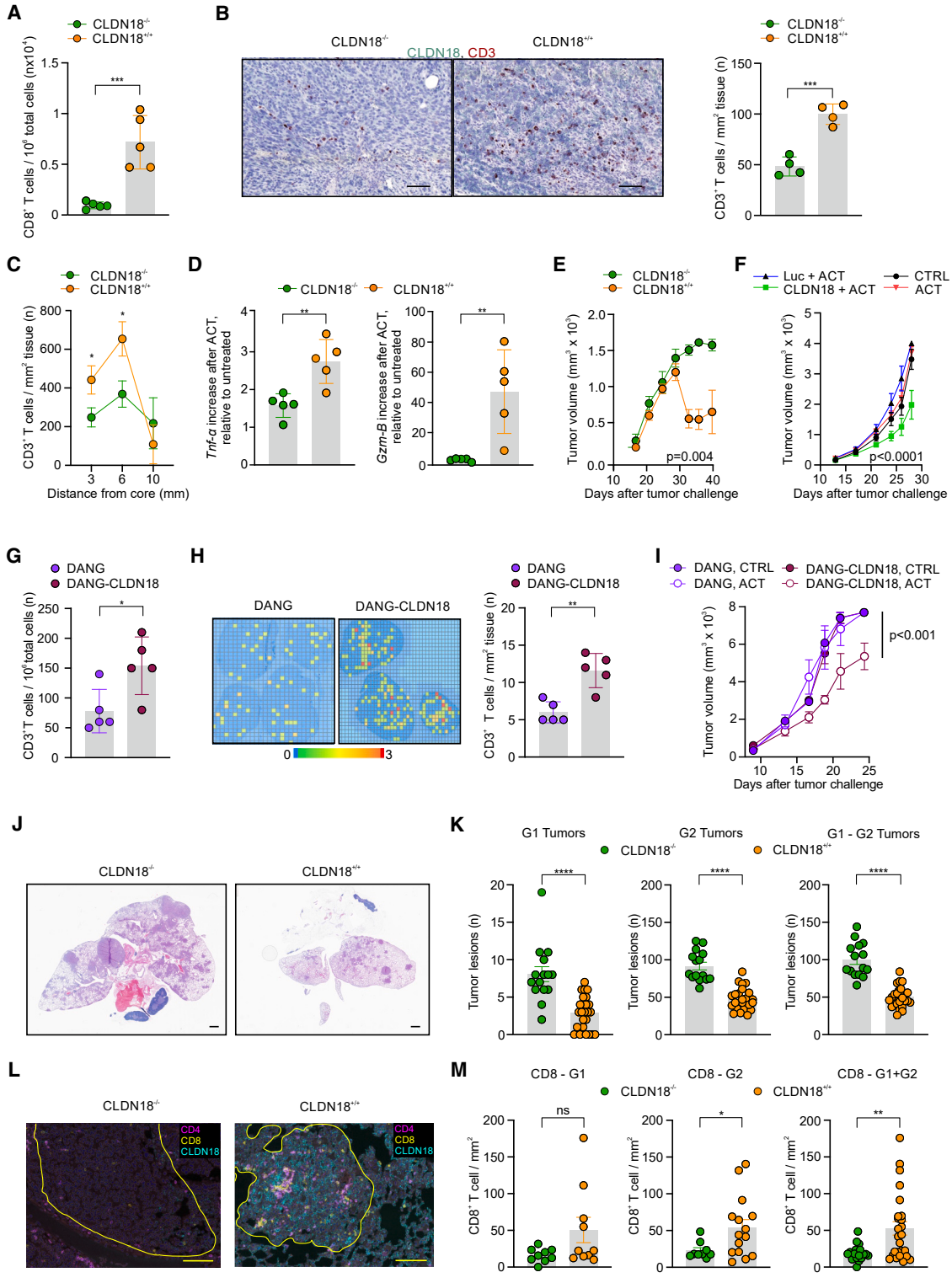

Figure 4. CLDN18 ablation reduces tumor immunity

(A) FC CD8$^+$ TIL quantification in immunodeficient mice (Rag2$^{-/-}$) bearing CLDN18$^{+/+}$ and CLDN18$^{-/-}$ FC1199-OVA tumors, euthanized 3 days after ACT with OVA-specific CTLs. Data are presented as mean ± SD. Unpaired, two-tailed t test. ***$p < 0.001$

(B) IHC images (left) showing CLDN18 in green and CD3 in red, scale bars, 100 μm; CD3$^+$ T cell quantification (right). Data are presented as mean ± SD. Unpaired, two-tailed t test. ***$p < 0.001$

(legend continued on next page)

tumor-bearing, immunodeficient Rag2$^{-/-}$ mice. Lack of CLDN18 was associated with looser interactions between T lymphocytes and tumor cells (Figure 5A), resulting in CTLs with broader and faster movement trajectories in CLDN18$^{-/-}$ than in CLDN18$^{+/+}$ tumors (Figure 5B; Videos S1 and S2), which suggests a role for CLDN18 in enhancing T lymphocyte-tumor cell interactions. *In vitro* assessment of CTL motility behavior in time-lapse confirmed a stronger interaction of T lymphocytes in the presence of CLDN18 on the tumor cell surface (Figure 5C), which in turn supported more robust immunological synapse (IS) formation between T lymphocytes and CLDN18$^{+/+}$ target cells compared with CLDN18$^{-/-}$ tumor cells (Figures 5D and S6A). *In vitro*, time course analysis of the intracellular release of calcium in CTLs as a proxy signal for TCR-mediated T cell activation[40] during the interaction with either CLDN18$^{+/+}$ or CLDN18$^{-/-}$ FC1199-OVA clones (Figure S6B) showed a significantly higher IS formation rate in CTLs cultured with CLDN18$^{+/+}$ cells (Figure 5E). The higher frequency of IS formation in the presence of CLDN18 was associated with increased release of cytokines that support the infiltration and function of CTLs in the tumor core. We found that increased CTL activation upon co-culture with CLDN18$^{+/+}$ tumor cells resulted in enhanced release of IFN-γ (Figure 5F), IL-3, CXC chemokine ligand 10 (CXCL10), and chemokine ligand 5 (CCL5) cytokines (Figure S6C) and enhanced cytotoxicity (Figure 5G).

We excluded that CLDN18-dependent interaction and activation of T lymphocytes relied on differential antigen processing and presentation ability, as similar results were obtained by pulsing CLDN18$^{+/+}$ and CLDN18$^{-/-}$ FC1199-OVA clones with the "SIINFEKL" OVA peptide (Figure S6D).

Actin-driven recruitment of ALCAM into lipid rafts by CLDN18 promotes IS formation and CTL infiltration into tumors

CLDN18 is involved in homotypic interactions[41]; however, both quiescent and activated CTLs do not express CLDN18 (Figure S7A), suggesting a different mechanism of interaction with tumor cells. We speculated that cancer cell expressing CLDN18 might stabilize T lymphocyte-tumor interactions by regulating the expression, or membrane accessibility of other adhesion molecules on tumor cells.

FC analysis showed that the FC1199-OVA cell line expressed higher levels of ALCAM, E-cadherin, and intercellular adhesion molecule 1 (ICAM-1) on the membrane as compared with the FC1242-OVA cell line (Figure 6A). Among adhesion molecules, only ALCAM was differentially expressed between the membranes of FC1199-OVA CLDN18$^{+/+}$ and CLDN18$^{-/-}$ tumor cells, as detected by extracellular FC staining and confirmed by surface immunofluorescence (IF) staining (Figures 6B, 6C, S7B, and S7C). Molecular (microarray, not shown) and proteomic data (Figure 6D) showed no differences in total ALCAM protein content between FC1199-OVA and FC1242-OVA tumor cells, suggesting a role for CLDN18 in regulating ALCAM distribution and localization to the cell membrane. We performed confocal microscopy analysis of CLDN18, ALCAM, and other adhesion molecules in FC1199-OVA cells and confirmed greater colocalization of CLDN18 with ALCAM than ICAM-1 on the cell membrane (Figure S7D).

ALCAM promotes IS formation and downstream CTL activation by locating to functional membrane domains, i.e., lipid rafts, and binding to its cognate receptor CD6 on CD8$^+$ T lymphocytes[42]; we thus asked whether CLDN18 might be involved in the formation of this receptor-receptor interaction. We isolated lipid rafts from monolayers of FC1242 cells expressing histidine (His)-tagged CLDN18 by collecting ten fractions after density gradient separation. Lipid rafts were identified by the presence of high levels of cholesterol, phospholipids, and caveolin and low actin levels[43] in fractions three and four of the density gradient separation (Figure S7E). We found ALCAM and CLDN18 to be co-localized in these fractions. We quantified the immunoblot data of fraction three from plasma membrane purification of either CLDN18$^{+/+}$ or CLDN18$^{-/-}$ FC1199-OVA tumor cells. The amount of ALCAM in the lipid raft isolates from CLDN18$^{+/+}$ FC1199-OVA was considerably higher

(C) Quantification of CD3$^+$ T cells infiltrating the tumor mass according to the distance from the center of the tumor (refer to STAR Methods). Data are presented as mean ± SD. Two-way ANOVA. *$p < 0.05$.
(D) Real-time PCR for *Tnf-α* and *Gzm-B* on mRNA extracted from whole tumors isolated from immunodeficient mice (Rag2$^{-/-}$) bearing CLDN18$^{+/+}$ and CLDN18$^{-/-}$ FC1199-OVA tumors, euthanized 3 days after ACT with OVA-specific CTL. Data are presented as mean ± SD. Unpaired, two-tailed t test. **$p < 0.01$.
(E) Tumor growth curve of immunodeficient mice bearing CLDN18$^{+/+}$ and CLDN18$^{-/-}$ FC1199-OVA tumors, receiving ACT of OVA-specific CTLs. Data are presented as mean ± SEM. Two-way ANOVA.
(F) Tumor growth curves in immunodeficient Rag2$^{-/-}$ mice challenged with CLDN18-deficient FC1242-OVA tumor cells, *in situ* transduced with GFP-luciferase (Luc) as control virus, GFP-CLDN18 (CLDN18) expressing viral particles or saline (CTRL) and adoptively transferred with OVA-specific CD8$^+$ CTLs (ACT). ****$p \leq 0.0001$.
(G) FC quantification of CD3$^+$ hTERT-specific TILs in immunodeficient NOG mice bearing CLDN18$^{+/+}$ and CLDN18$^{-/-}$ human DANG tumors 3 days after ACT. *$p = 0.02$.
(H) Heatmap plots (left) showing the localization (left) and quantification (right) of CD3$^+$ T cells (IHC) in DANG and DANG-CLDN18 tumor tissues obtained from immunodeficient NOG mice treated as in (G). **$p = 0.002$.
(I) Tumor growth curve of immunodeficient NOG mice bearing either DANG or DANG-CLDN18 that either received or not ACT with hTERT-specific CTLs (n = 5/group).
(J) H&E representative staining of the lung lobes isolated from CLDN18$^{+/+}$ and CLDN18$^{-/-}$ KP mouse lung lesions, 18 weeks after nose instillation with LentiCRE lentivirus (scale bars, 1 mm).
(K) Comparison of grade 1 (left), grade 2 (center), and grade 1 + grade 2 (right) tumor lesions in CLDN18$^{+/+}$ and CLDN18$^{-/-}$ KP mouse lungs. Data are presented as mean ± SD. Unpaired, two-tailed t test. *$p < 0.05$; **$p < 0.01$; ****$p < 0.0001$.
(L) Immunofluorescence (IF) representative images of the lung lobes isolated from conditional CLDN18$^{+/+}$ and CLDN18$^{-/-}$ KP mice stained for CDLN18, CD8$^+$, and CD4$^+$ T lymphocytes (scale bars, 100 μm). The yellow line determines the region of interest (ROI) corresponding to grade 2 adenoma, as defined by the pathologist.
(M) CD8$^+$ T cell quantification by immunofluorescence (IF) in lung tissues from CLDN18$^{+/+}$ and CLDN18$^{-/-}$ KP mice. Data are presented as mean ± SD. Unpaired, two-tailed t test. (A, B, D, G, and H) and as mean ± SEM. Two-way ANOVA (C, F, and I) and as mean ± SEM. Mann-Whitney test, one tailed (K and M). Data are presented as mean ± SD. Unpaired, two-tailed t test. *$p < 0.05$; **$p < 0.01$; ****$p < 0.0001$.

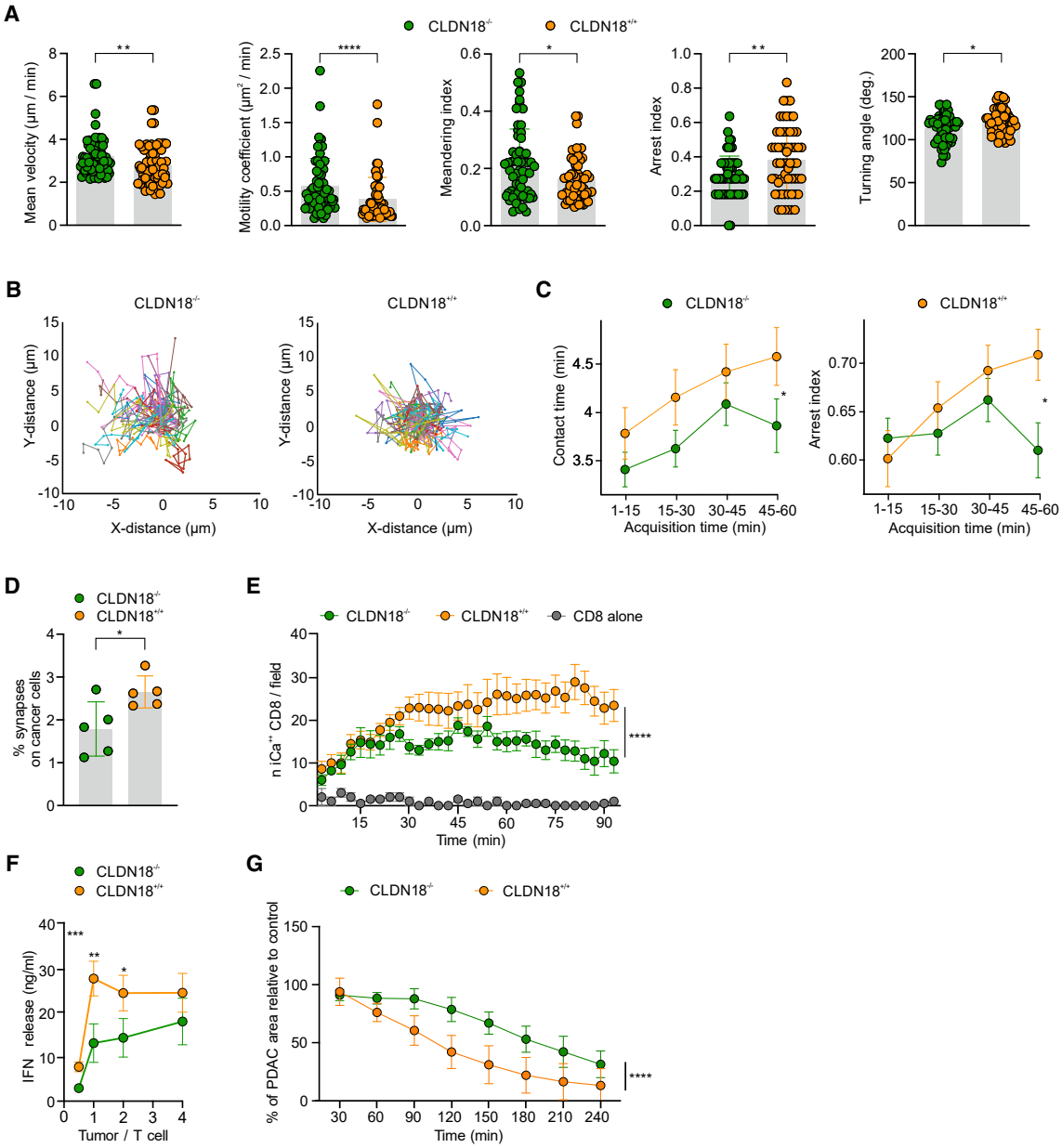

Figure 5. CLDN18 expression on tumor cells supports interaction with and activation of T lymphocytes

(A) Motility parameters referred as mean velocity, motility coefficient, meandering index, arrest index, and turning angle of tumor infiltrating, OVA-specific CTLs, evaluated *in vivo* by two-photon imaging in mice bearing either CLDN18$^{+/+}$ or CLDN18$^{-/-}$ FC1199-OVA tumors that received ACT with OVA-specific T cells. *$p \leq 0.05$, **$p = 0.006$, ****$p \leq 0.0001$.

(B) Bi-dimensional graph of OVA-specific CTL *in vivo* trajectories in CLDN18$^{+/+}$ and CLDN18$^{-/-}$ FC1199-OVA tumors, plotted from starting point (normalized as 0).

(C) *In vitro* kinetics of OVA-specific CTL interactions with CLDN18$^{+/+}$ and CLDN18$^{-/-}$ FC1199-OVA tumor cells. Contact time in minutes and arrest index were evaluated. Data are presented as mean ± SD. Mann-Whitney test, two tailed (A and C). *$p < 0.05$.

(D) Percentage of immunological synapses, defined as accumulation of CD3 at the point of contact between CTLs and either CLDN18$^{+/+}$ or CLDN18$^{-/-}$ FC1199-OVA tumor cells co-cultured at 1/1/1 ratio. Data are presented as mean ± SD. Unpaired, two-tailed t test. *$p = 0.03$.

(E) Immunofluorescent signal of intracellular Ca^{2+} levels of OVA-specific CTLs co-cultured with CLDN18$^{+/+}$ or CLDN18$^{-/-}$ FC1199-OVA tumor cells and acquired over time. CTLs were labeled with Ca^{2+} probe Biotracker 609 AM and immunofluorescent signal was followed over 90 min from the beginning of the co-culture and presented as number of Ca^{2+} CD8$^+$ T cells per field. Data are presented as mean ± SEM. Kruskal-Wallis test. ****$p \leq 0.0001$.

(F) IFN-γ quantification on the supernatant of CTLs co-cultured for 24 h with either CLDN18$^{+/+}$ or CLDN18$^{-/-}$ FC1199-OVA tumor cells. Data are presented as mean ± SEM. *$p < 0.05$; **$p < 0.01$; ***$p < 0.001$.

(G) Quantification in term of reduction of the area covered by either CLDN18$^{+/+}$ or CLDN18$^{-/-}$ FC1199-OVA tumor cells co-cultured with OVA-specific CTLs followed over 4 h from the beginning of the co-culture. Values are normalized to tumor cells alone. Data are presented as mean ± SD. Two-way ANOVA. ****$p \leq 0.0001$.

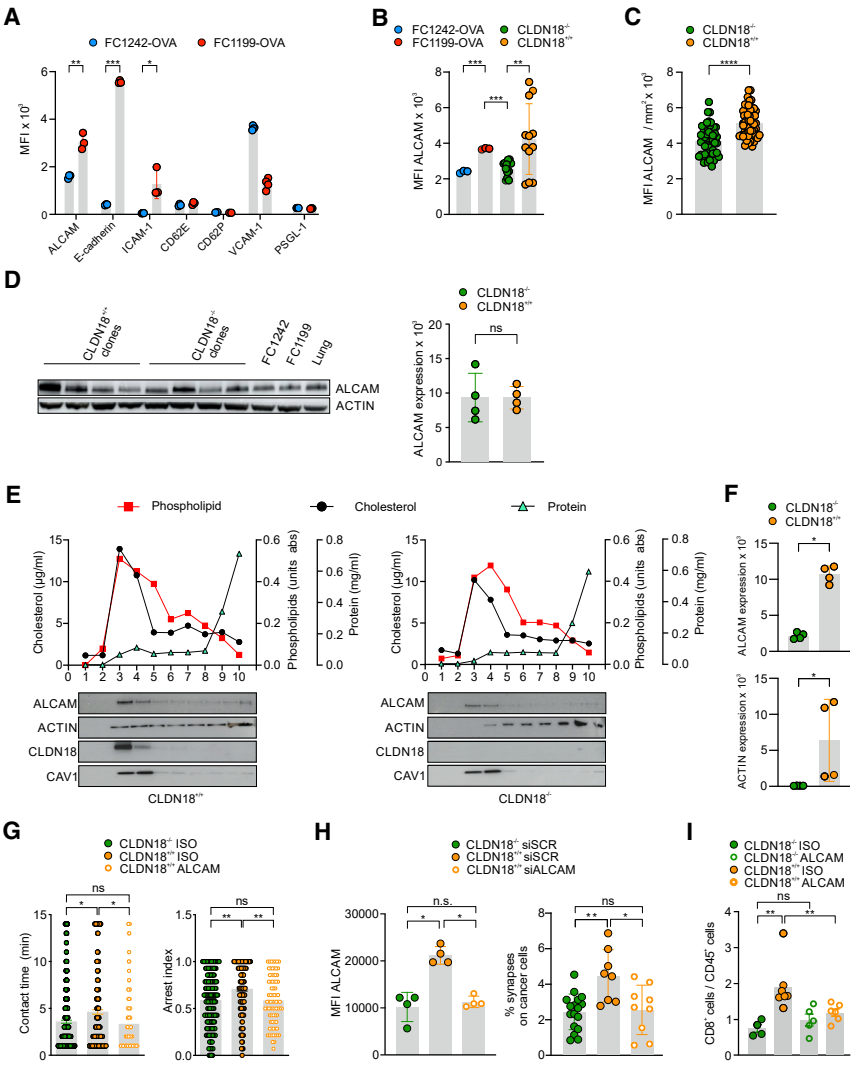

Figure 6. CLDN18 supports ALCAM localization on cell membrane and its accrual in lipid rafts

(A) FC quantification of adhesion molecules expressed on the cell membrane of FC1199-OVA and FC1242-OVA tumor cells. Data are presented as mean ± SD. Multiple t test.

(B) FC quantification of ALCAM cell surface expression on FC1242-OVA, FC1199-OVA, CLDN18$^{+/+}$, and CLDN18$^{-/-}$ FC1199-OVA cells. Data are presented as mean ± SD. Unpaired, two-tailed t test.

(C) IF quantification of ALCAM surface expression on FC1199-OVA CLDN18$^{+/+}$ or FC1199-OVA CLDN18$^{-/-}$ cell clones. ****$p \leq 0.0001$.

(D) Immunoblot (left) and quantification (right) of total ALCAM from CLDN18$^{+/+}$ and CLDN18$^{-/-}$ FC1199-OVA clones, FC1242 and FC1199 cell lines. Lung tissue is used as positive control for ALCAM. Actin shows equal loading. $p = 0.68$.

(E) Top: cholesterol, phospholipids, and total proteins were analyzed for each plasma membrane fraction (1–10) and for both CLDN18$^{+/+}$ (left) and CLDN18$^{-/-}$ FC1199-OVA cell lines (right). Bottom: immunoblots representing ALCAM, actin, CLDN18, and CAV1 of the 10 fractions obtained from plasma membrane purification isolated from CLDN18$^{+/+}$ (bottom left) and CLDN18$^{-/-}$ (bottom right) FC1199-OVA tumor cells.

(F) Densitometric quantification of ALCAM and actin in fraction three of plasma membrane of CLDN18$^{+/+}$ and CLDN18$^{-/-}$ FC1199-OVA tumor cells.

(G) *In vitro* kinetics of CTL interactions (parameters: contact time in minutes, and arrest index) with CLDN18$^{+/+}$ and CLDN18$^{-/-}$ tumor cells treated with blocking ALCAM antibody (ALCAM) or control isotype (Iso). Data are presented as mean ± SEM. Kruskal-Wallis test.

(H) FC evaluation of plasma membrane ALCAM expression after cell transfection with ALCAM-targeting siRNA (siALCAM) or irrelevant (siSCR) siRNA (left) and *in vitro* analysis of IS formation in CTLs (right). Data are presented as mean ± SD. Mann-Whitney test (C, D, F, and H). *$p = 0.02$, **$p = 0.007$.

(I) FC quantification of OVA-specific CD8$^+$ T cells in CLDN18$^{+/+}$ and CLDN18$^{-/-}$ FC1199-OVA tumor-bearing mice receiving ALCAM-blocking antibody (ALCAM) or isotype (Iso) before ACT with OVA-specific CTLs and euthanized 3 days later. Data are presented as mean ± SEM. Unpaired, two-tailed t test. When it is not specified, *$p < 0.05$; **$p < 0.01$; ***$p < 0.001$.

when compared with CLDN18$^{-/-}$ clones, thus suggesting that CLDN18 mediated the preferential ALCAM accrual in these functional membrane microdomains (Figures 6E and 6F). Actin was identified in fraction three of CLDN18$^{+/+}$ but not CLDN18$^{-/-}$ FC1199-OVA clone isolates, suggesting that CLDN18 drove ALCAM localization in lipid rafts through actin. Consistent with this hypothesis, immunoprecipitation with FC1242-CLDN18-His followed by western blot (WB) confirmed actin as an intracellular interactor of CLDN18 (Figure S7F).

In a time-lapse *in vitro* setting, we observed that ALCAM blockade by specific antibodies in CLDN18$^{+/+}$ FC1199-OVA tumor cells decreased CTL contact time and arrest index to the level of CLDN18$^{-/-}$ FC1199-OVA cells exposed to a control isotype antibody (Figure 6G). When ALCAM was silenced in CLDN18$^{+/+}$ FC1199-OVA tumor cells, both ALCAM membrane expression and IS formation in CTLs were no longer significantly different between CLDN18$^{+/+}$ and CLDN18$^{-/-}$ clones (Figure 6H). Quantification of OVA-specific CTLs following ACT in immunodeficient mice bearing either CLDN18$^{+/+}$ or CLDN18$^{-/-}$ FC1199-OVA tumors treated *in vivo* with either ALCAM-blocking antibodies or isotype controls demonstrated that ALCAM blockade undermined the advantage conferred by CLDN18 in driving CTLs to the tumor environment (Figure 6I). Considering that ALCAM can affect CTL activity by both homotypic (ALCAM-ALCAM) and heterotypic (ALCAM-CD6) binding, we sought to investigate which axis supported CTL interaction with tumor cells. We evaluated the dynamics of OVA-specific CTL contacts with PDAC cells during either dual ALCAM-ALCAM and ALCAM-CD6 binding blockade (anti-ALCAM) or selective CD6 blockade (by CD6 antagonist monoclonal antibody). ALCAM-ALCAM binding was crucial for initial T lymphocyte arrest on target cells, whereas ALCAM-CD6 interaction was negligible (Figure S7G). Nonetheless, ALCAM-CD6 blockade did play a role in downstream signaling following 24-h co-culture between T lymphocyte and tumor cells (Figure S7H). In fact, interference with CD6 binding resulted in IFN-γ release

reduction only in CTLs co-cultured with CLDN18$^{+/+}$ tumor cells (Figure S7H). Accordingly, CD6 blockade *in vivo* impaired T lymphocyte infiltration in CLDN18$^{+/+}$ tumors (Figure S7I). Thus, homotypic ALCAM interactions were important for the early CTL-tumor cell contacts, whereas binding of ALCAM to CD6 in T cells intervened in later steps of cell retention and activation.

Overall, these data confirmed a role for CLDN18 in supporting CTL interactions with tumor cells by driving ALCAM recruitment to lipid rafts in the cancer cell membrane through actin, thereby stabilizing IS formation and T cell activation.

DISCUSSION

Tumors employ multiple strategies to evade immune surveillance. Intrinsic and extrinsic immune evasion pathways include reduced antigenicity, low immunogenicity, and establishment of a highly suppressive TME through selective recruitment of regulatory myeloid and lymphoid cells at the expense of CTLs.[9,44,45] These strategies are all described in pancreatic cancer at the early stages of tumor progression, supported by oncogenic KRAS activation and genetic evolution, which underpin poor T cell infiltration and function against transformed epithelial cells.[8,46] During neoplastic transformation, the altered expression and cell surface localization of proteins involved in tissue architecture, such as CLDNs, may influence tissue scaffolding, epithelial polarity, and cell membrane composition.[47] CLDN expression and redirection from tight junctions to other membrane areas could therefore be an alarm signal for tissue damage.

Our results indicated that CLDN18 alerted the host immune system to T cell intervention. CLDN18 expression is transcriptionally regulated by the PKC/MAPK/AP-1-dependent pathway and maintained by epigenetic rewiring.[48] CLDN18 is tightly silenced on a transcriptional level in normal pancreatic cells. However, it can be promptly induced in the early stages of cancer development and later downregulated in PDAC. In agreement with Carpenter et al.,[49] we identified a stepwise alteration of CLDN18 expression in normal tissue transiting to PanIN and PDAC. Our study provided a mechanistic ground for these observations, by identifying in CLDN18 loss a driver of altered tumor immune contexture and patients' survival. We demonstrated that the presence of CLDN18 is associated with TIL localization in human PanINs, and LUAD, and is prognostic for better OS in PDAC and LUAD. A recent dataset of spatial transcriptomics in PDAC shows that the classical PDAC subtype expressing *CLDN18* is associated with CD4 T cells (but not T regulatory [Treg]) infiltration.[50] We replicated this analysis in published PDAC RNA-seq datasets,[17] but we could not confirm a similar correlation (data not shown). Moreover, our CD3$^+$ T lymphocyte infiltration assessment on 148 human PDAC samples (Figure 3) did not detect a direct association between CLDN18 and overall TILs (data not shown), suggesting that whole T lymphocyte numbers and CLDN18 may represent two variables with distinct impact on survival. However, we demonstrated that spatial localization within the tumor was crucial. Indeed, T lymphocytes were preferentially placed close to CLDN18$^+$ tumor cells in human PDAC, and CLDN18 strengthened T lymphocyte-tumor cell interactions in mouse tumor models of PDAC and LUAD, supporting CTL infiltration, ACT efficacy, and tumor-specific T cell immunity. In accordance, CLDN18 expression in conjunction with TILs stratified patients with better clinical performance suggesting that these two variables may be additive for patient prognosis. These findings prompted a reconsideration of the current view of PDAC as a tumor in which immune editing does not occur[45,51] and offer a new perspective for a selective pressure by T cells in selecting CLDN18 downregulation to allow the progression of early lesions. Lack of CLDN18 allowed escape from adhesion, recognition, and antitumor activity of CTLs. Thus, down-modulation of CLDN18 in pancreatic and lung cancers can be associated with evasion from immune recognition and the establishment of an immune-privileged environment.

We demonstrated *in vivo* and *in vitro* that CLDN18 leveraged immune cell interactions by strengthening the contacts between T lymphocytes and tumor cells, leading to the formation of IS, cytotoxicity, and cytokine release in activated T cells. The increased release in IFN-γ, CXCL10, CCL5, and TNF-α could further promote the recruitment of T cells to the tumor core.[52–55]

CLDN18 can regulate membrane localization and lipid raft assembly of membrane proteins.[19] We unveiled that CLDN18 formed supramolecular complexes with adhesion molecules and intracellular cytoskeletal proteins stabilizing ALCAM in lipid rafts, which supported stable IS formation between neoplastic cells and tumor-specific CTLs. Immunoprecipitation experiments identified actin as a direct intracellular binder of CLDN18. Together with other cytoskeletal structures, actin may support lipid raft assembly and movement by localizing within lipids and membrane proteins (including adhesion molecules and occludins) and regulating their lateral diffusion, following the model of a "fence post."[56]

ALCAM establishes not only homotypic binding to ALCAM but also heterotypic interactions with CD6 on T cell membrane.[57] These binding partners co-localize at the center of the IS and physically interact with the TCR complex, enhancing T cell activation.[42,58] We used ALCAM-specific siRNAs and ALCAM antibodies to block both homotypic and heterotypic interactions or anti-CD6 antibodies to restrain heterotypic interactions only and demonstrated that ALCAM was the key partner of CLDN18 to affect CTL functions, both *in vitro* and *in vivo*. ALCAM-ALCAM and ALCAM-CD6 mediated different, likely sequential steps during CTL early interactions and activation and were both crucial in supporting CD8$^+$ T cell trafficking within the TME.

CLDN18 intervenes in the early stages of PDAC progression, likely before other evasive mechanisms are established by the increasing cancer clonal diversification and its composite impact on the immunosuppressive TME. Additionally, TME evolution and tumor progression are profoundly affected by the site of tumor growth. Our results were in line with previous findings about a CTL-dependent immunoediting following subcutaneous injection of OVA-transduced KPC cell lines.[51] Subcutaneous tumor challenge allows better characterization of intrinsic tumor elusive strategies for T cell homing and activation, with a reduced interference of the stromal components fueling strong local immunosuppression in orthotopic models and autochthonous pancreatic tumors, especially in advanced stages.[9,11,59] Our findings in the subcutaneous PDAC models

were further confirmed in the orthotopic setting and autochthonous KP lung adenocarcinoma,[38] highlighting the early involvement of CLDN18 in the recognition of epithelial transformation by adaptive immunity.

CLDN18 is thus the precursor of a new class of proteins involved in CTL infiltration of tumors and is suitable for both patient stratification and therapeutic approaches. From a clinical perspective, these results place CLDN18 as a prognostic biomarker for improved survival and suggest that its regulated expression might endorse T cell infiltration and improve cancer immunotherapy.

Limitations of the study

Our data shed light on an immunoregulatory function of tight junction CLDN18 element, which could be exploited to improve further the efficacy of immunotherapy in cancer patients. Despite these intriguing insights, the study cannot rule out the presence of unforeseen interactions of CLDN18 with additional ligands on CTLs, and we did not unveil the contribution of other members of the CLDN family that are upregulated in $TILs^{hi}$ vs. $TILs^{lo}$ tumors. Finally, addressing the immunoregulatory role of CLDN18 on other innate and adaptive immune cell subsets is expected to provide important insights into the mechanisms of cancer immunology, further improving immunotherapy treatment responses.

STAR★METHODS

Detailed methods are provided in the online version of this paper and include the following:

- KEY RESOURCES TABLE
- RESOURCE AVAILABILITY
  - Lead contact
  - Materials availability
  - Data and code availability
- EXPERIMENTAL MODEL AND STUDY PARTICIPANT DETAILS
  - Patients
  - Mice
- METHOD DETAILS
  - Cell lines and culture conditions
  - CRISPR and single-cell-derived clone preparation
  - Activated OVA-specific CTL preparation
  - Expansion of mTERT-specific CTLs
  - Generation of hTERT-specific T cells
  - Lentivirus-mediated transduction in tumor cells
  - siRNA silencing
  - *In vivo* tumor models
  - *In vivo* treatments
  - Intratumoral pH measurement
  - Ultrasound imaging
  - Bioluminescence imaging
  - Preparation of cell suspensions from mouse organs
  - Functional assays
  - Adhesion assay with spheroids
  - T cell migration assay
  - Competition immunological synapse formation
  - Molecular analysis
  - Flow cytometry
  - Proteomic studies
  - Live Imaging
  - Histopathology analysis and digital image analysis
  - Immunofluorescence and digital image analysis
- QUANTIFICATION AND STATISTICAL ANALYSIS

SUPPLEMENTAL INFORMATION

Supplemental information can be found online at https://doi.org/10.1016/j.immuni.2024.04.021.

ACKNOWLEDGMENTS

We thank all members of the Immunology Section (in particular Dr. Nicolas Binetti, Dr. Gian Marco Ciresola, and Dr. Francesca Tregnaghi) of the University of Verona and the Histology core team at BioNTech for technical support in the realization of the project. Moreover, we acknowledge Dr. David Tuveson for supplying KPC-derived cell lines. We deeply acknowledge the contribution of "Centro Piattaforme Tecnologiche" of the University of Verona for imaging and molecular experiments and "Centro Interdipartimentale di Servizio alla Ricerca Sperimentale" of the University of Verona for maintaining mouse colonies. We thank Biorender for graphical abstract generation. We acknowledge cBioPortal for genome annotations of *CLDN18* gene in available PDAC datasets. Funding: this work was jointly supported by Cancer Research Institute (CRI, CLIP PI: V.B., project CRI3118); Associazione Italiana per la Ricerca sul Cancro (AIRC, PI: V.B., project 23788; PI: S.U., project: 21509; PI: A.S., project: 26343); PRIN programs of the Italian Ministry of Education, University, and Research (MIUR, PI: V.B., CUP: B38D19000260006; PI: S.U., CUP: B38D19000140006; PI: F.D.S., CUP: B39J22001200001); PNRR program project: MAD-2022-12375871 (PI: V.B., CUP J93C22002250006), and PNRR project MNESYS PE00000006 (PI: G.C., CUP: B33C22001060002). This research was also funded by Italian Ministry of Health Ricerca Corrente.

AUTHOR CONTRIBUTIONS

Conceptualization, F.D.S. and V.B.; investigation, F.D.S. and S.D.; formal analysis, F.D.S., S. Caligola, V.P., B.R., M.E., A.M.S., and T.M.; methodology, F.D.S., S. Caligola, C.A., V.P., S.W., A.M.S., B.R., T.M., K.S., P.B., F.B., R.G., and S. Canè; data curation, F.D.S.; project development, F.D.S. and V.B.; supervision and administration, F.D.S. and V.B.; manuscript writing - review and editing, F.D.S., S.D., and C.A.; formal analysis methodology, S.D. and G.A.; methodology and assay development, M.E.; resources, Z.B., C.H., R.L., V.C., A.S., G.C., F.V., U.S., Ö.T., and V.B.; supervision, S.U., U.S., and Ö.T.; manuscript review, S.U.; manuscript writing and editing, Ö.T.; funding acquisition, V.B.; manuscript editing, V.B.

DECLARATION OF INTERESTS

V.B. reports past personal fees from Codiak BioSciences and IO Biotech ApS outside of the submitted work. U.S. and Ö.T. are co-founders and respectively Chief Executive Officer and Chief Medical Officer of BioNTech AG, Mainz Germany and shareholders in the privately owned BioNTech AG as mentioned in the affiliation. F.D.S., M.E., and V.B. hold proprietary rights on the patent application no. PCT/EP2023/058504: "Methods for predicting and improving the therapeutic efficacy of cancer treatments and methods for cancer prognosis."

Received: May 24, 2023
Revised: January 30, 2024
Accepted: April 23, 2024
Published: May 14, 2024

REFERENCES

1. McGranahan, N., Furness, A.J.S., Rosenthal, R., Ramskov, S., Lyngaa, R., Saini, S.K., Jamal-Hanjani, M., Wilson, G.A., Birkbak, N.J., Hiley, C.T., et al. (2016). Clonal neoantigens elicit T cell immunoreactivity and sensitivity to immune checkpoint blockade. Science *351*, 1463–1469. https://doi.org/10.1126/science.aaf1490.
2. Rizvi, N.A., Hellmann, M.D., Snyder, A., Kvistborg, P., Makarov, V., Havel, J.J., Lee, W., Yuan, J., Wong, P., Ho, T.S., et al. (2015). Cancer immunology. Mutational landscape determines sensitivity to PD-1 blockade in non-small cell lung cancer. Science *348*, 124–128. https://doi.org/10.1126/science.aaa1348.

3. Snyder, A., Makarov, V., Merghoub, T., Yuan, J., Zaretsky, J.M., Desrichard, A., Walsh, L.A., Postow, M.A., Wong, P., Ho, T.S., et al. (2014). Genetic basis for clinical response to CTLA-4 blockade in melanoma. N. Engl. J. Med. *371*, 2189–2199. https://doi.org/10.1056/NEJMoa1406498.

4. Bruni, D., Angell, H.K., and Galon, J. (2020). The immune contexture and Immunoscore in cancer prognosis and therapeutic efficacy. Nat. Rev. Cancer *20*, 662–680. https://doi.org/10.1038/s41568-020-0285-7.

5. Tumeh, P.C., Harview, C.L., Yearley, J.H., Shintaku, I.P., Taylor, E.J.M., Robert, L., Chmielowski, B., Spasic, M., Henry, G., Ciobanu, V., et al. (2014). PD-1 blockade induces responses by inhibiting adaptive immune resistance. Nature *515*, 568–571. https://doi.org/10.1038/nature13954.

6. O'Reilly, E.M., Oh, D.Y., Dhani, N., Renouf, D.J., Lee, M.A., Sun, W., Fisher, G., Hezel, A., Chang, S.C., Vlahovic, G., et al. (2019). Durvalumab with or without tremelimumab for patients with metastatic pancreatic ductal adenocarcinoma: A Phase 2 randomized clinical trial. JAMA Oncol. *5*, 1431–1438. https://doi.org/10.1001/jamaoncol.2019.1588.

7. Rahib, L., Smith, B.D., Aizenberg, R., Rosenzweig, A.B., Fleshman, J.M., and Matrisian, L.M. (2014). Projecting cancer incidence and deaths to 2030: the unexpected burden of thyroid, liver, and pancreas cancers in the United States. Cancer Res. *74*, 2913–2921. https://doi.org/10.1158/0008-5472.CAN-14-0155.

8. Balachandran, V.P., Beatty, G.L., and Dougan, S.K. (2019). Broadening the impact of immunotherapy to pancreatic cancer: challenges and opportunities. Gastroenterology *156*, 2056–2072. https://doi.org/10.1053/j.gastro.2018.12.038.

9. Hegde, S., Krisnawan, V.E., Herzog, B.H., Zuo, C., Breden, M.A., Knolhoff, B.L., Hogg, G.D., Tang, J.P., Baer, J.M., Mpoy, C., et al. (2020). Dendritic cell paucity leads to dysfunctional immune surveillance in pancreatic cancer. Cancer Cell *37*, 289–307.e9. https://doi.org/10.1016/j.ccell.2020.02.008.

10. Clark, C.E., Hingorani, S.R., Mick, R., Combs, C., Tuveson, D.A., and Vonderheide, R.H. (2007). Dynamics of the immune reaction to pancreatic cancer from inception to invasion. Cancer Res. *67*, 9518–9527. https://doi.org/10.1158/0008-5472.CAN-07-0175.

11. De Sanctis, F., Lamolinara, A., Boschi, F., Musiu, C., Caligola, S., Trovato, R., Fiore, A., Frusteri, C., Anselmi, C., Poffe, O., et al. (2022). Interrupting the nitrosative stress fuels tumor-specific cytotoxic T lymphocytes in pancreatic cancer. J. Immunother. Cancer *10*, e003549. https://doi.org/10.1136/jitc-2021-003549.

12. Beatty, G.L., Chiorean, E.G., Fishman, M.P., Saboury, B., Teitelbaum, U.R., Sun, W., Huhn, R.D., Song, W., Li, D., Sharp, L.L., et al. (2011). CD40 agonists alter tumor stroma and show efficacy against pancreatic carcinoma in mice and humans. Science *331*, 1612–1616. https://doi.org/10.1126/science.1198443.

13. Panni, R.Z., Herndon, J.M., Zuo, C., Hegde, S., Hogg, G.D., Knolhoff, B.L., Breden, M.A., Li, X., Krisnawan, V.E., Khan, S.Q., et al. (2019). Agonism of CD11b reprograms innate immunity to sensitize pancreatic cancer to immunotherapies. Sci. Transl. Med. *11*, eaau9240. https://doi.org/10.1126/scitranslmed.aau9240.

14. Padrón, L.J., Maurer, D.M., O'Hara, M.H., O'Reilly, E.M., Wolff, R.A., Wainberg, Z.A., Ko, A.H., Fisher, G., Rahma, O., Lyman, J.P., et al. (2022). Sotigalimab and/or nivolumab with chemotherapy in first-line metastatic pancreatic cancer: clinical and immunologic analyses from the randomized phase 2 PRINCE trial. Nat. Med. *28*, 1167–1177. https://doi.org/10.1038/s41591-022-01829-9.

15. Collisson, E.A., Sadanandam, A., Olson, P., Gibb, W.J., Truitt, M., Gu, S., Cooc, J., Weinkle, J., Kim, G.E., Jakkula, L., et al. (2011). Subtypes of pancreatic ductal adenocarcinoma and their differing responses to therapy. Nat. Med. *17*, 500–503. https://doi.org/10.1038/nm.2344.

16. Moffitt, R.A., Marayati, R., Flate, E.L., Volmar, K.E., Loeza, S.G.H., Hoadley, K.A., Rashid, N.U., Williams, L.A., Eaton, S.C., Chung, A.H., et al. (2015). Virtual microdissection identifies distinct tumor- and stroma-specific subtypes of pancreatic ductal adenocarcinoma. Nat. Genet. *47*, 1168–1178. https://doi.org/10.1038/ng.3398.

17. Bailey, P., Chang, D.K., Nones, K., Johns, A.L., Patch, A.M., Gingras, M.C., Miller, D.K., Christ, A.N., Bruxner, T.J.C., Quinn, M.C., et al. (2016). Genomic analyses identify molecular subtypes of pancreatic cancer. Nature *531*, 47–52. https://doi.org/10.1038/nature16965.

18. Suzuki, H., Nishizawa, T., Tani, K., Yamazaki, Y., Tamura, A., Ishitani, R., Dohmae, N., Tsukita, S., Nureki, O., and Fujiyoshi, Y. (2014). Crystal structure of a claudin provides insight into the architecture of tight junctions. Science *344*, 304–307. https://doi.org/10.1126/science.1248571.

19. Hagen, S.J., Ang, L.H., Zheng, Y., Karahan, S.N., Wu, J., Wang, Y.E., Caron, T.J., Gad, A.P., Muthupalani, S., and Fox, J.G. (2018). Loss of tight junction protein claudin 18 promotes progressive neoplasia development in mouse stomach. Gastroenterology *155*, 1852–1867. https://doi.org/10.1053/j.gastro.2018.08.041.

20. Hayashi, D., Tamura, A., Tanaka, H., Yamazaki, Y., Watanabe, S., Suzuki, K., Suzuki, K., Sentani, K., Yasui, W., Rakugi, H., et al. (2012). Deficiency of claudin-18 causes paracellular H+ leakage, up-regulation of interleukin-1beta, and atrophic gastritis in mice. Gastroenterology *142*, 292–304. https://doi.org/10.1053/j.gastro.2011.10.040.

21. Wöll, S., Schlitter, A.M., Dhaene, K., Roller, M., Esposito, I., Sahin, U., and Türeci, Ö. (2014). Claudin 18.2 is a target for IMAB362 antibody in pancreatic neoplasms. Int. J. Cancer *134*, 731–739. https://doi.org/10.1002/ijc.28400.

22. Tallent, A. (2023). Zolbetuximab improves survival in gastric cancer. Cancer Discov. *13*, 520–521. https://doi.org/10.1158/2159-8290.CD-NB2023-0006.

23. Qi, C., Gong, J., Li, J., Liu, D., Qin, Y., Ge, S., Zhang, M., Peng, Z., Zhou, J., Cao, Y., et al. (2022). Claudin18.2-specific CAR T cells in gastrointestinal cancers: phase 1 trial interim results. Nat. Med. *28*, 1189–1198. https://doi.org/10.1038/s41591-022-01800-8.

24. Reinhard, K., Rengstl, B., Oehm, P., Michel, K., Billmeier, A., Hayduk, N., Klein, O., Kuna, K., Ouchan, Y., Wöll, S., et al. (2020). An RNA vaccine drives expansion and efficacy of claudin-CAR-T cells against solid tumors. Science *367*, 446–453. https://doi.org/10.1126/science.aay5967.

25. Hingorani, S.R., Wang, L., Multani, A.S., Combs, C., Deramaudt, T.B., Hruban, R.H., Rustgi, A.K., Chang, S., and Tuveson, D.A. (2005). Trp53R172H and KrasG12D cooperate to promote chromosomal instability and widely metastatic pancreatic ductal adenocarcinoma in mice. Cancer Cell *7*, 469–483. https://doi.org/10.1016/j.ccr.2005.04.023.

26. Li, J., Byrne, K.T., Yan, F., Yamazoe, T., Chen, Z., Baslan, T., Richman, L.P., Lin, J.H., Sun, Y.H., Rech, A.J., et al. (2018). Tumor cell-intrinsic factors underlie heterogeneity of immune cell infiltration and response to immunotherapy. Immunity *49*, 178–193.e7. https://doi.org/10.1016/j.immuni.2018.06.006.

27. Hänzelmann, S., Castelo, R., and Guinney, J. (2013). GSVA: gene set variation analysis for microarray and RNA-seq data. BMC Bioinformatics *14*, 7. https://doi.org/10.1186/1471-2105-14-7.

28. Quan, M.Y., Guo, Q., Liu, J., Yang, R., Bai, J., Wang, W., Cai, Y., Han, R., Lv, Y.Q., Ding, L., et al. (2020). An FGFR/AKT/SOX2 signaling axis controls pancreatic cancer stemness. Front. Cell Dev. Biol. *8*, 287. https://doi.org/10.3389/fcell.2020.00287.

29. Luo, L., Sun, W., Zhu, W., Li, S., Zhang, W., Xu, X., Fang, D., Grahn, T.H.M., Jiang, L., and Zheng, Y. (2021). BCAT1 decreases the sensitivity of cancer cells to cisplatin by regulating mTOR-mediated autophagy via branched-chain amino acid metabolism. Cell Death Dis. *12*, 169. https://doi.org/10.1038/s41419-021-03456-7.

30. Principe, D.R., DeCant, B., Mascariñas, E., Wayne, E.A., Diaz, A.M., Akagi, N., Hwang, R., Pasche, B., Dawson, D.W., Fang, D., et al. (2016). TGFbeta signaling in the pancreatic tumor microenvironment promotes fibrosis and immune evasion to facilitate tumorigenesis. Cancer Res. *76*, 2525–2539. https://doi.org/10.1158/0008-5472.CAN-15-1293.

31. Blasco, M.T., Navas, C., Martín-Serrano, G., Graña-Castro, O., Lechuga, C.G., Martín-Díaz, L., Djurec, M., Li, J., Morales-Cacho, L., Esteban-Burgos, L., et al. (2019). Complete regression of advanced pancreatic

ductal adenocarcinomas upon combined inhibition of EGFR and C-RAF. Cancer Cell *35*, 573–587.e6. https://doi.org/10.1016/j.ccell.2019.03.002.

32. Cancer Genome Atlas Research, N. (2017). Integrated Genomic Characterization of Pancreatic Ductal Adenocarcinoma. Cancer Cell *32*, 185–203.e13. https://doi.org/10.1016/j.ccell.2017.07.007.
33. Chen, F., Zhang, Y., Parra, E., Rodriguez, J., Behrens, C., Akbani, R., Lu, Y., Kurie, J.M., Gibbons, D.L., Mills, G.B., et al. (2017). Multiplatform-based molecular subtypes of non-small-cell lung cancer. Oncogene *36*, 1384–1393. https://doi.org/10.1038/onc.2016.303.
34. Sandri, S., De Sanctis, F., Lamolinara, A., Boschi, F., Poffe, O., Trovato, R., Fiore, A., Sartori, S., Sbarbati, A., Bondanza, A., et al. (2017). Effective control of acute myeloid leukaemia and acute lymphoblastic leukaemia progression by telomerase specific adoptive T-cell therapy. Oncotarget *8*, 86987–87001. https://doi.org/10.18632/oncotarget.18115.
35. Sandri, S., Bobisse, S., Moxley, K., Lamolinara, A., De Sanctis, F., Boschi, F., Sbarbati, A., Fracasso, G., Ferrarini, G., Hendriks, R.W., et al. (2016). Feasibility of telomerase-specific adoptive T-cell therapy for B-cell chronic lymphocytic leukemia and solid malignancies. Cancer Res. *76*, 2540–2551. https://doi.org/10.1158/0008-5472.CAN-15-2318.
36. Cheng, H., Qiu, Y., Xu, Y., Chen, L., Ma, K., Tao, M., Frankiw, L., Yin, H., Xie, E., Pan, X., et al. (2023). Extracellular acidosis restricts one-carbon metabolism and preserves T cell stemness. Nat. Metab. *5*, 314–330. https://doi.org/10.1038/s42255-022-00730-6.
37. Feng, Q., Liu, Z., Yu, X., Huang, T., Chen, J., Wang, J., Wilhelm, J., Li, S., Song, J., Li, W., et al. (2022). Lactate increases stemness of CD8 + T cells to augment anti-tumor immunity. Nat. Commun. *13*, 4981. https://doi.org/10.1038/s41467-022-32521-8.
38. DuPage, M., Cheung, A.F., Mazumdar, C., Winslow, M.M., Bronson, R., Schmidt, L.M., Crowley, D., Chen, J., and Jacks, T. (2011). Endogenous T cell responses to antigens expressed in lung adenocarcinomas delay malignant tumor progression. Cancer Cell *19*, 72–85. https://doi.org/10.1016/j.ccr.2010.11.011.
39. Nikitin, A.Y., Alcaraz, A., Anver, M.R., Bronson, R.T., Cardiff, R.D., Dixon, D., Fraire, A.E., Gabrielson, E.W., Gunning, W.T., Haines, D.C., et al. (2004). Classification of proliferative pulmonary lesions of the mouse: recommendations of the mouse models of human cancers consortium. Cancer Res. *64*, 2307–2316. https://doi.org/10.1158/0008-5472.can-03-3376.
40. Joseph, N., Reicher, B., and Barda-Saad, M. (2014). The calcium feedback loop and T cell activation: how cytoskeleton networks control intracellular calcium flux. Biochim. Biophys. Acta *1838*, 557–568. https://doi.org/10.1016/j.bbamem.2013.07.009.
41. Krause, G., Winkler, L., Mueller, S.L., Haseloff, R.F., Piontek, J., and Blasig, I.E. (2008). Structure and function of claudins. Biochim. Biophys. Acta *1778*, 631–645. https://doi.org/10.1016/j.bbamem.2007.10.018.
42. Zimmerman, A.W., Joosten, B., Torensma, R., Parnes, J.R., van Leeuwen, F.N., and Figdor, C.G. (2006). Long-term engagement of CD6 and ALCAM is essential for T-cell proliferation induced by dendritic cells. Blood *107*, 3212–3220. https://doi.org/10.1182/blood-2005-09-3881.
43. Cayrol, R., Wosik, K., Berard, J.L., Dodelet-Devillers, A., Ifergan, I., Kebir, H., Haqqani, A.S., Kreymborg, K., Krug, S., Moumdjian, R., et al. (2008). Activated leukocyte cell adhesion molecule promotes leukocyte trafficking into the central nervous system. Nat. Immunol. *9*, 137–145. https://doi.org/10.1038/ni1551.
44. Sharma, P., Hu-Lieskovan, S., Wargo, J.A., and Ribas, A. (2017). Primary, adaptive, and acquired resistance to cancer immunotherapy. Cell *168*, 707–723. https://doi.org/10.1016/j.cell.2017.01.017.
45. Vonderheide, R.H. (2018). The immune revolution: A case for priming, not checkpoint. Cancer Cell *33*, 563–569. https://doi.org/10.1016/j.ccell.2018.03.008.
46. Dias Carvalho, P., Guimarães, C.F., Cardoso, A.P., Mendonça, S., Costa, Â.M., Oliveira, M.J., and Velho, S. (2018). KRAS oncogenic signaling extends beyond cancer cells to orchestrate the microenvironment. Cancer Res. *78*, 7–14. https://doi.org/10.1158/0008-5472.CAN-17-2084.
47. Li, J. (2021). Context-dependent roles of claudins in tumorigenesis. Front. Oncol. *11*, 676781. https://doi.org/10.3389/fonc.2021.676781.
48. Ito, T., Kojima, T., Yamaguchi, H., Kyuno, D., Kimura, Y., Imamura, M., Takasawa, A., Murata, M., Tanaka, S., Hirata, K., and Sawada, N. (2011). Transcriptional regulation of claudin-18 via specific protein kinase C signaling pathways and modification of DNA methylation in human pancreatic cancer cells. J. Cell. Biochem. *112*, 1761–1772. https://doi.org/10.1002/jcb.23095.
49. Carpenter, E.S., Elhossiny, A.M., Kadiyala, P., Li, J., McGue, J., Griffith, B.D., Zhang, Y., Edwards, J., Nelson, S., Lima, F., et al. (2023). Analysis of donor pancreata defines the transcriptomic signature and microenvironment of early neoplastic lesions. Cancer Discov. *13*, 1324–1345. https://doi.org/10.1158/2159-8290.CD-23-0013.
50. Hwang, W.L., Jagadeesh, K.A., Guo, J.A., Hoffman, H.I., Yadollahpour, P., Reeves, J.W., Mohan, R., Drokhlyansky, E., Van Wittenberghe, N., Ashenberg, O., et al. (2022). Single-nucleus and spatial transcriptome profiling of pancreatic cancer identifies multicellular dynamics associated with neoadjuvant treatment. Nat. Genet. *54*, 1178–1191. https://doi.org/10.1038/s41588-022-01134-8.
51. Evans, R.A., Diamond, M.S., Rech, A.J., Chao, T., Richardson, M.W., Lin, J.H., Bajor, D.L., Byrne, K.T., Stanger, B.Z., Riley, J.L., et al. (2016). Lack of immunoediting in murine pancreatic cancer reversed with neoantigen. JCI Insight *1*, e88328. https://doi.org/10.1172/jci.insight.88328.
52. Ozga, A.J., Chow, M.T., and Luster, A.D. (2021). Chemokines and the immune response to cancer. Immunity *54*, 859–874. https://doi.org/10.1016/j.immuni.2021.01.012.
53. Huffman, A.P., Lin, J.H., Kim, S.I., Byrne, K.T., and Vonderheide, R.H. (2020). CCL5 mediates CD40-driven CD4+ T cell tumor infiltration and immunity. JCI Insight *5*, e137263. https://doi.org/10.1172/jci.insight.137263.
54. Facciabene, A., De Sanctis, F., Pierini, S., Reis, E.S., Balint, K., Facciponte, J., Rueter, J., Kagabu, M., Magotti, P., Lanitis, E., et al. (2017). Local endothelial complement activation reverses endothelial quiescence, enabling T-cell homing, and tumor control during T-cell immunotherapy. Oncoimmunology *6*, e1326442. https://doi.org/10.1080/2162402X.2017.1326442.
55. De Sanctis, F., Ugel, S., Facciponte, J., and Facciabene, A. (2018). The dark side of tumor-associated endothelial cells. Semin. Immunol. *35*, 35–47. https://doi.org/10.1016/j.smim.2018.02.002.
56. Head, B.P., Patel, H.H., and Insel, P.A. (2014). Interaction of membrane/lipid rafts with the cytoskeleton: impact on signaling and function: membrane/lipid rafts, mediators of cytoskeletal arrangement and cell signaling. Biochim. Biophys. Acta *1838*, 532–545. https://doi.org/10.1016/j.bbamem.2013.07.018.
57. Hassan, N.J., Barclay, A.N., and Brown, M.H. (2004). Frontline: Optimal T cell activation requires the engagement of CD6 and CD166 FrontLine. Eur. J. Immunol. *34*, 930–940. https://doi.org/10.1002/eji.200424856.
58. Gimferrer, I., Calvo, M., Mittelbrunn, M., Farnós, M., Sarrias, M.R., Enrich, C., Vives, J., Sánchez-Madrid, F., and Lozano, F. (2004). Relevance of CD6-mediated interactions in T cell activation and proliferation. J. Immunol. *173*, 2262–2270. https://doi.org/10.4049/jimmunol.173.4.2262.
59. Freed-Pastor, W.A., Lambert, L.J., Ely, Z.A., Pattada, N.B., Bhutkar, A., Eng, G., Mercer, K.L., Garcia, A.P., Lin, L., Rideout, W.M., 3rd, et al. (2021). The CD155/TIGIT axis promotes and maintains immune evasion in neoantigen-expressing pancreatic cancer. Cancer Cell *39*, 1342–1360.e14. https://doi.org/10.1016/j.ccell.2021.07.007.
60. Willrodt, A.H., Salabarria, A.C., Schineis, P., Ignatova, D., Hunter, M.C., Vranova, M., Golding-Ochsenbein, A.M., Sigmund, E., Romagna, A., Strassberger, V., et al. (2019). ALCAM mediates DC migration through afferent lymphatics and promotes allospecific immune reactions. Front. Immunol. *10*, 759. https://doi.org/10.3389/fimmu.2019.00759.
61. Dull, T., Zufferey, R., Kelly, M., Mandel, R.J., Nguyen, M., Trono, D., and Naldini, L. (1998). A third-generation lentivirus vector with a conditional packaging system. J Virol *72*, 8463–8471. https://doi.org/10.1128/JVI.72.11.8463-8471.1998.

62. Türeci, Ö., Mitnacht-Kraus, R., Wöll, S., Yamada, T., and Sahin, U. (2019). Characterization of zolbetuximab in pancreatic cancer models. Oncoimmunology *8*, e1523096. https://doi.org/10.1080/2162402X.2018.1523096.

63. Zhou, B., Flodby, P., Luo, J., Castillo, D.R., Liu, Y., Yu, F.X., McConnell, A., Varghese, B., Li, G., Chimge, N.O., et al. (2018). Claudin-18-mediated YAP activity regulates lung stem and progenitor cell homeostasis and tumorigenesis. J Clin Invest *128*, 970–984. https://doi.org/10.1172/JCI90429.

64. Motz, G.T., Santoro, S.P., Wang, L.P., Garrabrant, T., Lastra, R.R., Hagemann, I.S., Lal, P., Feldman, M.D., Benencia, F., and Coukos, G. (2014). Tumor endothelium FasL establishes a selective immune barrier promoting tolerance in tumors. Nat Med *20*, 607–615. https://doi.org/10.1038/nm.3541.

65. Irizarry, R.A., Bolstad, B.M., Collin, F., Cope, L.M., Hobbs, B., and Speed, T.P. (2003). Summaries of Affymetrix GeneChip probe level data. Nucleic Acids Res. *31*, e15. https://doi.org/10.1093/nar/gng015.

66. Bolstad, B.M., Irizarry, R.A., Astrand, M., and Speed, T.P. (2003). A comparison of normalization methods for high density oligonucleotide array data based on variance and bias. Bioinformatics *19*, 185–193. https://doi.org/10.1093/bioinformatics/19.2.185.

67. Irizarry, R.A., Hobbs, B., Collin, F., Beazer-Barclay, Y.D., Antonellis, K.J., Scherf, U., and Speed, T.P. (2003). Exploration, normalization, and summaries of high density oligonucleotide array probe level data. Biostatistics *4*, 249–264. https://doi.org/10.1093/biostatistics/4.2.249.

68. Ritchie, M.E., Phipson, B., Wu, D., Hu, Y., Law, C.W., Shi, W., and Smyth, G.K. (2015). limma powers differential expression analyses for RNA-sequencing and microarray studies. Nucleic Acids Res. *43*, e47. https://doi.org/10.1093/nar/gkv007.

69. Dennis, G., Jr., Sherman, B.T., Hosack, D.A., Yang, J., Gao, W., Lane, H.C., and Lempicki, R.A. (2003). DAVID: Database for Annotation, Visualization, and Integrated Discovery. Genome Biol. *4*, P3.

70. Ramos, M., Geistlinger, L., Oh, S., Schiffer, L., Azhar, R., Kodali, H., de Bruijn, I., Gao, J., Carey, V.J., Morgan, M., and Waldron, L. (2020). Multiomic integration of public oncology databases in bioconductor. JCO Clin. Cancer Inform. *4*, 958–971. https://doi.org/10.1200/CCI.19.00119.

71. Gu, Z., Eils, R., and Schlesner, M. (2016). Complex heatmaps reveal patterns and correlations in multidimensional genomic data. Bioinformatics *32*, 2847–2849. https://doi.org/10.1093/bioinformatics/btw313.

72. Rooney, M.S., Shukla, S.A., Wu, C.J., Getz, G., and Hacohen, N. (2015). Molecular and genetic properties of tumors associated with local immune cytolytic activity. Cell *160*, 48–61. https://doi.org/10.1016/j.cell.2014.12.033.

73. Mennuni, C., Ugel, S., Mori, F., Cipriani, B., Iezzi, M., Pannellini, T., Lazzaro, D., Ciliberto, G., La Monica, N., Zanovello, P., et al. (2008). Preventive vaccination with telomerase controls tumor growth in genetically engineered and carcinogen-induced mouse models of cancer. Cancer Res. *68*, 9865–9874. https://doi.org/10.1158/0008-5472.CAN-08-1603.

74. Love, M.I., Huber, W., and Anders, S. (2014). Moderated estimation of fold change and dispersion for RNA-seq data with DESeq2. Genome Biol. *15*, 550. https://doi.org/10.1186/s13059-014-0550-8.

75. Durinck, S., Moreau, Y., Kasprzyk, A., Davis, S., De Moor, B., Brazma, A., and Huber, W. (2005). BioMart and Bioconductor: a powerful link between biological databases and microarray data analysis. Bioinformatics *21*, 3439–3440. https://doi.org/10.1093/bioinformatics/bti525.

76. Dusi, S., Angiari, S., Pietronigro, E.C., Lopez, N., Angelini, G., Zenaro, E., Della Bianca, V., Tosadori, G., Paris, F., Amoruso, A., et al. (2019). LFA-1 controls Th1 and Th17 motility behavior in the inflamed central nervous system. Front. Immunol. *10*, 2436. https://doi.org/10.3389/fimmu.2019.02436.

77. Zenaro, E., Rossi, B., Angiari, S., and Constantin, G. (2013). Use of imaging to study leukocyte trafficking in the central nervous system. Immunol. Cell Biol. *91*, 271–280. https://doi.org/10.1038/icb.2012.81.

STAR★METHODS

KEY RESOURCES TABLE

REAGENT or RESOURCE	SOURCE	IDENTIFIER
Antibodies		
Anti TERT (clone Y182)	Novus Biologicals	Cat#NB 120-32020 RRID:AB_1193246
Anti 6x-His Tag (clone HIS.H8)	Invitrogen™	Cat#MA1-21315 RRID: AB_557403
Anti ALCAM	Invitrogen™	Cat#PA5-47083 RRID:AB_2607383
Anti Caveolin 1	Invitrogen™	Cat#PA1-064 RRID:AB_2072027
Anti β-Actin HRP conjugate (clone 8H10D10)	Cell Signaling Technology	Cat# 12262 RRID:AB_2566811
Anti Claudin 18	Invitrogen™	Cat#38-8100 RRID:AB_2932564
Anti IgG HRP conjugate	Santa Cruz Biotechnology	Cat#sc-2354 RRID:AB_628490
Anti IgG HRP-linked F(ab')$_2$ fragment	Cytiva	Cat#NA9340 RRID:AB_772191
Anti human CD3 (clone OKT-3)	eBioscience™	Cat#14-0037-82 RRID:AB_467057
Anti human IFN-γ (clone B27)	BD Pharmingen™	Cat#554701 RRID:AB_395518
Anti mouse CD3 (clone17A2)	eBioscience™	Cat#14-0032-82 RRID:AB_467053
Anti mouse H-2Kd (clone SF1-1.1)	Biolegend	Cat#116617 RRID:AB_10612575
Anti mouse ICAM1 (clone YN1/1.7.4)	Biolegend	Cat#116119 RRID:AB_10613645
Anti mouse ALCAM (clone eBioALC48)	eBioscience™	Cat#12-1661-82 RRID:AB_823125
Anti E-Cadherin (clone DECMA-1)	eBioscience™	Cat#50-3249-82 RRID:AB_11040003
Anti CD62P (clone Psel.KO2.3)	eBioscience™	Cat#46-0626-82 RRID: AB_2573688
Anti mouse VCAM1 (clone 429)	BD Pharmingen™	Cat# 553332 RRID:AB_394784
Anti mouse PSGL-1 (clone 4RA10)	eBioscience™	Cat# 46-1621-80 RRID: AB_2848337
Anti human CD3 (clone SK7)	BD Pharmingen™	Cat# 557832 RRID:AB_396890
Anti mouse CD3 (clone 17A2)	Sony Biotechnology	Cat# 1101140
Anti GAPDH HRP conjugated (clone14C10)	Cell Signaling Technology	Cat#3683 RRID:AB_1642205
Anti human TERT (clone Y182)	Abcam	Cat# Ab 32020 RRID:AB_778296
Anti mouse TCR V beta 5.1/5.2 (clone MR9-4)	eBioscience™	Cat# 46-5796-82 RRID:AB_2762644
Anti-ALCAM (I/F8-Fc bivalent Fc fusion protein)	C. Halin et al.	Willrodt et al.[60]

(*Continued on next page*)

Continued

REAGENT or RESOURCE	SOURCE	IDENTIFIER
Isotype control (KSF-Fc bivalent Fc fusion protein)	C. Halin et al.	Willrodt et al.[60]
Anti Ovalbumin	Invitrogen™	Cat#PA1-196 RRID:AB_2539921
Anti mouse/human CD11b (clone M1/70)	Biolegend	Cat#101263 RRID:AB_2629529
Anti mouse CD45 (clone 30F-11)	Biolegend	Cat#103138 RRID:AB_2563061
Anti mouse CD8a (clone 53-6.7)	Biolegend	Cat#100702 RRID:AB_312741
Imab 362	Ö. Türeci and U. Sahin et al.	Wöll et al.[21]
LIVE/DEAD™ Fixable Green Dead Cell Stain Kit	Invitrogen™	Cat#L23101
LIVE/DEAD™ Fixable Aqua Dead Cell Stain Kit	Invitrogen™	Cat#L34966
Anti human CD3 (clone SP34-2)	BD Pharmingen™	Cat#552127 RRID:AB_394342
Mouse IgG	Vector Laboratories	Cat#I-2000 RRID:AB_2336354
Anti CD3 (clone SP7)	Abcam	Cat#AB16669 RRID:AB_443425
Anti-rabbit HRP	Invitrogen™	Cat # 31460 RRID: AB_228341
Anti Claudin18 (clone 43-14A)	Ganymed	N/A
Anti human CD4 (clone SP35)	Roche Ventana	Cat#790-4423 RRID:AB_2335982
Anti human CD3 (clone 2GV6)	Roche Ventana	Cat#790-4341 RRID:AB_2335978
Anti human CD8 (clone SP16)	Novus Biologicals	Cat#NB019410
OmniMap anti rabbit HRP	Roche Ventana	Cat#760-4311 RRID:AB_2811043
OmniMap anti mouse HRP	Roche Ventana	Cat#760-4310 RRID:AB_2885182
anti mouse Claudin18 (clone 34H14L15)	Invitrogen™	Cat#700178 RRID:AB_2532290
Anti mouse CD4 (clone 766)	Sino Biological	Cat#50134-R766 RRID:AB_2857993
Anti mouse anti CD8 (clone 4SM15)	eBioscience™	Cat#14-0808-82 RRID:AB_2572861
OmniMap anti rat HRP	Roche Ventana	Cat#760-4457
Donkey anti-Goat IgG (H+L)	Invitrogen™	Cat#A32860 RRID:AB_2762841
Goat anti-Human IgG (H+L)	Invitrogen™	Cat#A48275 RRID:AB_2890321
Goat anti-Rat IgG (H+L)	Invitrogen™	Cat#A48261 RRID:AB_2890550
Biotin Rat Anti-Mouse IFN-γ (clone XMG1.2)	BD Biosciences	Cat#554410 RRID:AB_395374
Anti-CD6 Purified Rat Monoclonal IgG	R&D System	Cat#MAB7271 RRID:AB_1964534
Isotype control anti-HRPN	BioXCell	Cat#BP0088
Bacterial and virus strains		
One Shot™ TOP10 Chemically Competent E. coli	Invitrogen™	Cat#C404010
pRSV-Rev	Didier Trono	Addgene #12253[61]

(*Continued on next page*)

Continued

REAGENT or RESOURCE	SOURCE	IDENTIFIER
pMDLg/pRRE	Didier Trono	Addgene #12251[61]
pMD2.G	Didier Trono	Addgene #12259
Biological samples		
Primary Tumor PDAC tissue	ARCNET laboratory	N/A
Primary Tumor PanIN tissue	ARCNET laboratory	N/A
Chemicals, peptides, and recombinant proteins		
Brij® 58	Merck	Cat#P5884
Complete™ Protease Inhibitor Cocktail	Merck	Cat#11697498001
Halt™ Phosphatase Inhibitor Single-Use Cocktail	Thermo Scientific™	Cat#78428
RIPA Lysis and Extraction Buffer	Thermo Scientific™	Cat#89901
Viromer® RED	Lipocalyx	Cat#VR-01LB-00
Human recombinant IL-2	Prepotech	Cat#200-02
AIM V™ Medium	Gibco™	Cat#12055091
Normal Human Serum	Invitrogen™	Cat#31876
Human recombinant IL-15	Miltenyi Biotec	Cat#130-095-762
Polybrene Infection / Transfection Reagent	Merck	Cat#TR-1003-G
Collagenase type I	Merck	Cat#1148089
Collagenase type II	Merck	Cat#1148090
Collagenase type IV	Merck	Cat#C4-22
DNAse I	Merck	Cat#260913
Elastase	Worthington Biochemical	Cat#LS-02292
OVA257-264 peptide H-SIINFEKL-OH	JPT	N/A
Concanavalin A	Merck	Cat#C5275
AKP Streptavidin	BD Pharmingen™	Cat#554065
Vector NovaRED® Substrate Kit, Peroxidase (HRP)	Vector laboratories	Cat#SK-4800
Chromium-51 Radionuclide	Perkin – Elmer	Cat#NEZ030S001MC
hTERT peptide RLVDDFLIV-OH	JPT	N/A
mTERT198-205 peptide VGRNFTNL-OH	JPT	N/A
CellTrace™ Violet Cell Proliferation Kit	Invitrogen™	Cat#C34557
RPMI 1640 no phenol red	Gibco™	Cat#11835-063
Nunc™ Lab-Tek™ II Chamber Slide™ System	Thermo Scientific™	Cat#154534
Matrigel® Growth Factor Reduced (GFR) Basement Membrane Matrix	Corning®	Cat#354230
DAPI	Merck	Cat#D9542
Normal goat serum	Vector Laboratories	Cat#S-1000-20
RNAlater™ Stabilization Solution	Invitrogen™	Cat#AM7021
SYBR® Green PCR Master Mix	Applied Biosystems™	Cat#4309155
BioTracker 609 Red Ca2+ AM dye	Merck	Cat#SCT021
PKH26 Red Fluorescent Cell Linker Kit for General Cell Membrane Labeling	Merck	Cat#PKH26GL-1KT
CellTracker™ Blue CMAC Dye	Invitrogen™	Cat#C2110
Permanent HRP Green	Zytomed Systems	Cat#ZYT-ZUC070-100
ProLong™ Gold Antifade Mountant	Invitrogen™	Cat#P36930

(*Continued on next page*)

Continued

REAGENT or RESOURCE	SOURCE	IDENTIFIER
Alexa Fluor™ 647 Phalloidin	Thermo Scientific™	Cat#A22287 RRID:AB_2620155
Critical commercial assays		
Pierce™ BCA Protein Assay Kit - Reducing Agent Compatible	Thermo Scientific™	Cat#23250
Phospholipid Assay Kit (Colorimetric/ Fluorimetric)	Abcam	Cat#ab234050
Amplex Red Cholesterol Assay Kit	Invitrogen™	Cat#A12216
Mouse IFNg uncoated ELISA Kit	Invitrogen™	Cat#88-7314-88
DuoSet Mouse IL-3	R&D Systems	Cat#DY403
DuoSet Mouse CXCL10/IP-10/CRG-2	R&D Systems	Cat#DY466
DuoSet CCL5/RANTES	R&D Systems	Cat#DY478
RNeasy Mini Kit	Qiagen	Cat#74104
RNase-Free DNase Set	Qiagen	Cat#79254
RevertAid RT Reverse Transcription Kit	Thermo Scientific™	Cat#K1691
Wonder RT cDNA Synthesis kit	Euroclone	Cat#EME037050
LookOut Mycoplasma PCR Detection kit	Merck	Cat#MP0035
CD34 MicroBead Kit, human	Milltenyi Biotech	Cat#130-046-702
TransIT®-mRNA Transfection Kit	Myrus Bio	Cat#MIR 2250
Foxp3 / Transcription Factor Staining Buffer Set	eBioscience™	Cat#00-5523-00
Deposited data		
Microarray data	This paper	GEO. GSE230868
Experimental models: Cell lines		
293 [HEK-293]	ATCC	Cat#CRL-1573™ RRID:CVCL_9804
FC1199	D. Tuveson Laboratory	N/A
FC1242	D. Tuveson Laboratory	N/A
hTERT-specific T cells	S. Sandri et al.	Sandri at al.[35]
DANG	Ö. Türeci and U. Sahin	Türeci et al.[62]
DANG-CLDN18	Ö. Türeci and U. Sahin	Türeci et al.[62]
MBL-2 cells	ATCC	Cat#HB-193™ RRID:CVCL_G236
Experimental models: Organisms/strains		
Mouse: C57BL/6NCrl	Charles River Laboratory	Cat#C57BL/6NCrl RRID:MGI:2683688
Mouse: C57BL/6-Tg(TcraTcrb)1100Mjb/J	Jackson Laboratory	Cat#003831 RRID:IMSR_JAX:003831
Mouse: C57BL/6NTac.Cg-*Rag2*^{tm1Fwa} *Il2rg*^{tm1Wjl}	Taconic Biosciences	Cat#4111
Mouse: NOD Cg-PrkdcscidIl2rgtm 1 Sug/YicTac	Taconic Biosciences	Cat#NODSC
Mouse: LSL-Kras$^{G12D/+}$	The Jackson Laboratory	Strain #:008179 RRID:IMSR_JAX:008179
Mouse: LSL-Trp53$^{R172H/+}$	The Jackson Laboratory	Strain #:008652 RRID:IMSR_JAX:008652
Mouse: CLDN$^{flox/flox}$	Zea Borok	Zhou et al.[63]
Mouse: KPCldn$^{fl/fl}$ (LSL-Kras$^{G12D/+}$ LSL-Trp53$^{R172H/+}$ CLDN$^{flox/flox}$)	This paper	N/A

(*Continued on next page*)

Continued

REAGENT or RESOURCE	SOURCE	IDENTIFIER
Oligonucleotides		
siRNA targeting sequence: ALCAM CGAUGAGGCAGACGAUAUA GCAGUGGGAGCGUCAUAAA UGGCAGGUAUUAUAGUAAA GCACAAUAUCUGCAAGUAG	Horizon discovery	Cat# LQ-042896-00-0010
siRNa targeting sequence: SCRAMBLE UGGUUUACAUGUCGACUAA UGGUUUACAUGUUGUGUGA	Horizon discovery	Cat# D-001810-10-20
crRNA CRISPR CLDN18 GATGATCGTAGGCATCGTCC GCCCTGAAATGCATCCGCAT GCCAACATGACACTGACCTC	IDT Integrated DNA technologies	Alt-R® CRISPR-Cas9 crRNA
Cas9 protein	IDT Integrated DNA technologies	Cat# 1081058
trackRNA	IDT Integrated DNA technologies	Cat# 1072534
Recombinant DNA		
pELNS-OVA-GFP	G. Coukos et al.	Motz et al.[64]
Lenti-LucOS	Tyler Jacks	Addgene #22777 DuPage et al.[38]
pELNS-GFP-CLDN18-His	This paper	N/A
Software and algorithms		
Living Image Software 4.4	Perkin Elmer	https://resources.perkinelmer.com/corporate/content/lst_software_downloads/living_image_44_release_notes.pdf
Multichip Average Algorithm (RMA)	CRAN	Irizarry et al.[65]; Bolstad et al.[66]; Irizarry et al.[67]
Limma package	Bioconductor	Ritchie et al.[68]
DAVID web application	G.Dennis Jr et al.	Dennis et al.[69]
R package 'GSVA' 1.46.0	Bioconductor	Hänzelmann et al.[27]
R package 'rms' 6.5-0	CRAN	https://CRAN.R-project.org/package=maxstat
R package 'survival' 3.5-3	CRAN	https://CRAN.R-project.org/package=maxstat
R package 'maxstat' 0.7-2.5	CRAN	https://CRAN.R-project.org/package=maxstat
R package 'survminer' 0.4.9	CRAN	https://CRAN.R-project.org/package=survminer
R package 'RTCGA' 1.28.0	Github	https://rtcga.github.io/RTCGA
PAAD, LUAD and LUSC TCGA datasets	Cancer Genome Atlas Research Network	Cancer Genome Atlas Research, N.[32]
R package 'curatedTCGAData' 1.20.1	Bioconductor	Ramos et al.[70]
R package 'ggpubr' 0.6.0	N/A	https://CRAN.R-project.org/package=ggpubr
R package 'DESeq2' 1.38.3	Bioconductor	N/A
R package 'biomaRt' 2.54.0	Bioconductor	N/A
R package 'ComplexHeatmap' 2.14.0	Bioconductor	Gu et al.[71]
R package 'ggplot2' 3.4.1	CRAN	N/A
GSVA scores on immune gene sets	M S Rooney et al.	Rooney et al.[72]
GSVA scores on T cells low and T cell high tumor samples	J Li et al.	Li et al.[26]
FlowJo software	BD Biosciences	https://www.flowjo.com/solutions/flowjo/downloads
ImageJ software	Fiji	https://imagej.net/software/fiji/downloads

(*Continued on next page*)

Continued

REAGENT or RESOURCE	SOURCE	IDENTIFIER
Zen v3.5 software	Zeiss	https://www.zeiss.com/microscopy/en/products/software/zeiss-zen.html
GraphPad Prism	GraphPad	https://www.graphpad.com/features
Imaris software	Imaris	https://imaris.oxinst.com/

RESOURCE AVAILABILITY

Lead contact

Further information and requests for resources should be directed to and will be fulfilled by the lead contact, Vincenzo Bronte (vincenzo.bronte@iov.veneto.it).

Materials availability

All newly generated materials described in this manuscript, or sequences required for their recombinant production, can be shared upon reasonable request.

Data and code availability

- Microarray Affymetrix data have been deposited at GEO and are publicly available as of the date of publication. Accession numbers are listed in the key resources table.
- This paper does not report original code or structures.
- All data supporting the findings of this study are available within the paper and from the corresponding author upon request. Any additional information required to reanalyze the data reported in this paper is available from the lead contact upon request.

Data availability statement

All data relevant to the study are included in the article or uploaded as supplemental information. *Availability of data and materials.* The microarray data have been deposited in the Gene Expression Omnibus (GEO) under the accession code GSE230868. The authors declare that all other data supporting the findings of this study are available in the article and the supplemental files.

EXPERIMENTAL MODEL AND STUDY PARTICIPANT DETAILS

Patients

For the use of PDAC and HD samples, informed consent was obtained from all participants and the study was approved by the Ethics Committee: Prot. 25978, Prog. 2172 on 29/05/2012 from Comitato Etico per la sperimentazione clinica delle province di Verona e Rovigo; Principal investigator: Aldo Scarpa. Patients and/or the public were not involved in the design, or conduct, or reporting, or dissemination plans of this research.

Mice

C57Bl/6 mice were purchased from Charles River Laboratories Inc; TCR-transgenic mice C57BL/6-Tg(TcraTcrb)1100Mjb/J referred to as OT-1 mice were purchased from Jackson Laboratory (Bar Harbor, Maine, USA). B10;B6-*Rag2*^{tm1Fwa} *Il2rg*^{tm1Wjl} referred as Rag2$^{-/-}$ and NOD Cg-Prkdcscid Il2rgtm1Sug/JicTac referred to as NOG mice were purchased from Taconic Biosciences (NY, USA). An autochthonous model of immunogenic lung adenocarcinoma in CLDN18-proficient and CLDN18-deficient genetic backgrounds was developed in our laboratory. Briefly, we crossed *LSL-Kras*$^{G12D/+}$ and *LSL-Trp53*$^{R172H/+}$ with CLDN$^{flox/flox}$ mice to generate KPCldn$^{fl/fl}$ mice. In KPCldn$^{+/+}$ and KPCldn$^{fl/fl}$ mice, infection of lung cells resulted in activation of oncogenic Kras, loss of Trp53, and finally deletion of CLDN18 in floxed mice. All genetically transgenic mice and their respective controls were gender and age-matched (typically 8–10 weeks). Animals were maintained in individually ventilated cages and in pathogen-free conditions at the animal facility of the University of Verona under standardized conditions with a 12-h photoperiod and were provided with food and water *ad libitum*. All animal experiments were conducted according to national (protocol number 12722 approved by the Ministerial Decree Number 14/2012-B of January 18, 2012 and protocol number BR15/08 approved by the Ministerial Decree Number 925/2015-PR of August 28, 2015; Principal Investigator: Vincenzo Bronte) and European laws and regulations. All animal experiments were approved by Verona University Ethical Committee (http://www.medicina.univr.it/fol/main?ent=bibliocr&id=85) and conducted according to the guidelines of Federation of European Laboratory Animal Science Associations (FELASA). All animal experiments were in accordance with the Amsterdam Protocol on animal protection and welfare: mice were monitored daily and euthanized when displaying excessive discomfort.

METHOD DETAILS

Cell lines and culture conditions

Mouse FC1199 (H-2b) and FC1242 (H-2b) KPC-derived cell lines were kindly donated by Dr. D. Tuveson (Cold Spring Harbor Laboratory, NY, USA). FC1199, FC1242, as well as MBL-2 and HEK293 (ATCC- Manassas, VA), were cultured in high-glucose DMEM supplemented with 10% heat-inactivated fetal bovine serum, 2 mM L-glutamine, 10 mM HEPES, 10 mM sodium pyruvate, 150 U/ml streptomycin and 200 U/ml penicillin. hTERT-specific T cells or OT-I-derived splenocytes were respectively cultured in RPMI 1640 or high-glucose DMEM supplemented with 10% heat-inactivated fetal bovine serum, 2 mM L-glutamine, 10mM HEPES, 10 mM sodium pyruvate, 20 μM β-mercaptoethanol, 100 U/ml streptomycin, 100 U/ml penicillin and 0.1 mM MEM Non-Essential Amino Acid Solution. Human pancreatic cancer cell lines DANG and DANG-CLDN18 (overexpressing the isoform predominantly expressed in pancreatic cancers CLDN18.2) were previously described here.[62] Cell lines were cultured in RPMI 1640 supplemented with 10% heat-inactivated FBS, 2 mM L-glutamine, 10mM HEPES, 150 U/ml streptomycin and 200 U/ml penicillin. The cell culture medium for DANG-CLDN18 was additionally supplemented with 1 μg/ml blasticidin. All cell lines were thawed from primary stocks maintained under liquid nitrogen and cultured for a maximum of three weeks during which time all experiments were performed. All cell lines were cultured in a 5% CO2-humidified incubator at 37°C and routinely validated to be free from mycoplasma by PCR.

CRISPR and single-cell-derived clone preparation

For the CLDN18 knockout in FC1199-OVA cells, specific crRNA was designed, targeting the sequence in the second exon of the mouse CLDN18 gene, and purchased from Integrated DNA Technologies (IDT, Iowa, USA). Cas9 protein and tracrRNA were purchased from the same company. gRNA was prepared by mixing in equimolar ration crRNA and tracrRNA and incubation for 5 minutes at 95°C. Equimolar ratios of gRNA and Cas9 were mixed and incubated with Viromer CRISPR reagent for ribonucleoproteins (RNP) formation. The RNP complexes were added to FC1199-OVA cells, and the next day the cells were seeded in 96-well plates at 1 cell per well dilution. Single-cell-derived clones were detected and cultured for 2 weeks for amplification. CLDN18 loss was determined by FACS analysis.

Activated OVA-specific CTL preparation

Splenocytes from OT-I TCR transgenic mice were isolated by mechanical spleen smashing through a 70 μm nylon mesh filter to obtain a single-cell suspension. Briefly, 10 x 10^6 cells per well were cultured in a 24-well plate for three days in the presence of 1 μg/ml $OVA_{257-264}$ peptide (SIINFEKL), supplemented every day with fresh medium and 20 U/ml of human recombinant IL-2. OVA-specific CTLs were washed with culture medium on day four and maintained in resting conditions (culture medium supplemented with 20 U/ml of human recombinant IL-2) for the last 24h before the experiment. Purity of $CD8^+$ Vß5^+ CTLs was determined by FACS analysis (higher than 90%) on the day of the experiment.

Expansion of mTERT-specific CTLs

Polyclonal $mTERT_{198-205}$ CTLs were previously isolated from TERT-vaccinated mice splenocytes and expanded by co-culturing with irradiated, syngeneic splenocytes pulsed with 0.1 μM f $mTERT_{198-205}$ (VGRNFTNL) peptide in complete medium containing 20 IU/mL of recombinant human IL-2 (Miltenyi Biotec, Germany).[73]

Generation of hTERT-specific T cells

hTERT-specific T cells were generated as previously described.[35] AIM-V medium (Gibco) supplemented with 5% human serum (Gibco, Thermo Fisher Scientific, Waltham, MA, USA) was used for clone preparation and expansion. Briefly, PBMCs were activated on plates pre-coated with anti-CD3 activating antibody (Thermo Fisher Scientific) and infected with $hTERT_{865–873}$/PG13 cell-derived viral supernatant. Transduced cells were sorted with CD34-selection beads (Miltenyi Biotec, Germany) and expanded in the presence of 300 IU/ml human recombinant IL-2 (Miltenyi Biotec, Germany) and 100 μg/ml of human recombinant IL-15 (Miltenyi Biotec, Germany).

Lentivirus-mediated transduction in tumor cells

The lentiviral construct pELNS-OVA-GFP was kindly provided by Dr. G. Coukos group. CLDN18-His was subcloned in pELNS to generate pELNS-GFP-CLDN18-His. For virus productions HEK293 cells were used as packaging cells. The HIV-1 lentiviral packaging was performed in HEK293 cells, where lentiviral vectors along with pDEL, pREV, and VSV-G were delivered by incubation with 60 mM $CaCl_2$. Virus-containing supernatants were harvested 48 h after transfection, filtered with 0.22 μm-pored filters and concentrated by ultracentrifugation at 50.000 g for 2.20 h. Target cell lines were infected with MOI (multiplicity of infection) 2 in the presence of 8 μg/ml of polybrene (Millipore, Billerica, MA, USA) and subsequently cultured for 24 h at 37 °C. After 2 days of infection the cell lines were sorted twice for the enrichment of GFP-positive cells using a FACS Aria II Flow Cytometer Cell Sorter (BD Biosciences).

siRNA silencing

1x10^5 cancer cells were seeded in 24-well plates for 5h, before performing the transfection (TransIT-X2® - Myrus). After 45 hours, medium was replaced in each well with 450 μl of complete growth medium. Transfection mix comprises 50 μl Opti-MEM, 14 pmole

of ALCAM siRNA (siALCAM) or irrelevant siRNA (siSCR) and 1 μl of Transit. After incubation 50 μl of transfection mix was added per well, drop-wise and the next day 500 μl of complete medium was added on top. ALCAM silencing was evaluated by flow cytometry.

In vivo tumor models

$5x10^5$, $5x10^4$, $2x10^4$ tumor cells were used for subcutaneous, orthotopic and intravenous syngeneic tumor studies, respectively. Subcutaneous tumor growth was monitored every 2 days using a digital caliper and metastasis were evaluated by lung weight. The greatest longitudinal diameter (length) and the greatest transverse diameter (width) were determined and tumor volume was calculated by the modified ellipsoidal formula: tumor volume = 1/2 (length x width^2). $1x10^6$ tumor cells were subcutaneously injected in xenogeneic models (DANG, DANG-CLDN18 tumor cell lines).

In vivo treatments

Adoptive cell therapy

OVA-specific CTLs were adoptively transferred by intravenous injection in tumor bearing mice at dose comprised between $2x10^6$ and $1x10^5$ cells according to the experiment.

$1x10^7$ mTERT-specific CTLs, were adoptively transferred by intravenous injection in mice bearing orthotopic syngeneic CLDN18$^{+/+}$ and CLDN18$^{-/-}$ tumors followed by 60,000 U of IL-2, daily injected IP for three days, to support T cell viability. Treatments started one week after tumor challenge and were performed thrice (one/week) for therapeutic studies.

$5x10^6$ hTERT-specific T lymphocytes were adoptively transferred by intravenous injection in mice bearing human tumor cell lines. Treatment was repeated twice (one/week). To perform all the TILs studies, mice received only one ACT when tumor was established and were sacrificed three days following ACT to collect and process the tumors for immune phenotype analysis.

In vivo transduction

$5x10^6$ and $3x10^7$ pELNS-GFP-CLDN18-His lentivirus particles encoding a CLDN18-GFP fusion construct were intratumorally injected in FC1242-OVA tumor bearing mice.

For the lung adenocarcinoma mouse model, we activated Flox cassettes in epithelial lung cells by intranasal instillation of $5x10^6$ CRE lentivirus particles. We employed the ''lenti-CRE'' expressing only CRE or Lenti-lucOS (engineered to express firefly luciferase fused with the ''SIINFEKL" peptide of the OVA protein) to establish LUAD expressing or not CD8-restricted immunodominant OVA epitope recognized by CTLs.[38]

In vivo ALCAM and CD6 blockade

CLDN18$^{+/+}$ and CLDN18$^{-/-}$ tumor bearing mice were administrated 3 hours prior to ACT with 200 μg intraperitoneal plus 50 μg intratumor delivery of anti-ALCAM antibody (l/F8-Fc bivalent Fc fusion protein), monoclonal anti-CD6 antibody (Clone 96117, R&D) or isotype controls (KSF-Fc bivalent Fc fusion protein, clone HRPN BioXcell, for ALCAM and CD6 respectively).[60]

Intratumoral pH measurement

pH meter with a needle probe was used directly on tumors 14 days after injection.

Ultrasound imaging

High-resolution ultrasound imaging (Vevo 2100, FUJIFILM VisualSonics, Toronto, ON, Canada) was performed in a blinded fashion, and analysis was independently supervised by two investigators (F.D.S and S.D.). Tumor volume was estimated by measuring the 2 smallest and largest perpendicular dimensions (as for caliper measurements) and followed during disease progression.

Bioluminescence imaging

In the spontaneous and immunogenic model of lung adenocarcinoma in CLDN18 proficient and CLDN18$^{+/+}$ mice, tumor growth was recorded at sacrifice by bioluminescence imaging (BLI; photons/second/cm^2/sr) using the IVIS Spectrum Imaging System (Perkin Elmer, Waltham, MA, USA). Lung bioluminescence images were acquired *ex-vivo* and tumor burden was evaluated 18 weeks after viral instillation. The subsequent parameters were used: exposure time = 5 minutes, field of view = 19x19 cm, binning B = 8 and f/stop = 1. Images were quantified tracing the region of interest (ROI) on the entire animal body. Living Image Software 4.4 (Perkin Elmer, Waltham, MA, USA) was used to acquire and quantify the bioluminescence.

Preparation of cell suspensions from mouse organs

Donor tumor bearing mice were sacrificed and the spleens and tumors were collected and processed according to already published protocols.[54] Briefly, spleens were mechanically homogenized, red blood cells were lysed and cell suspensions were filtered on cell strainer (Corning Inc, New York, USA) to remove aggregates. Tumors were finely cut and enzymatically digested with a solution containing 75 mg/ml collagenase type I, 75 mg/ml collagenase type II, 50 mg/ml collagenase type IV, 10 mg/ml DNAse I and 10 mg/ml elastase in DMEM medium for 1 hour at 37°C pipetting every 15 minutes. Tumor cell suspension was separated from aggregates by 70 μm cell strainer filtration, washed with complete DMEM media and, if necessary, depleted of red blood cells. Finally, cells were utilized for flow cytometry staining.

Functional assays

Tumor cell line proliferation assay

FC1199, FC1199-OVA, FC1242 and FC1242-OVA cells were seeded in 6-well plates at concentration of $2.5x10^5$ cells/well. Every 24h cell number was assessed by detaching cells and counterstaining the dead cells with trypan blue solution (Lonza).

ELISPOT

Donor tumor bearing mice were euthanized and the spleens were harvested four days after ACT. Single-cell suspensions of splenocytes were used for anti-IFN-γ ELISPOT assay, as previously described.[54] Briefly, 10^6 splenocytes were seeded on IFNγ-precoated (BD PharMingen) 96-well MAIP plates (Millipore) and incubated at 37°C for 20 h with 1 μg/mL OVA peptide or control H-2Kb-restricted peptide mTERT198-205. Concanavalin A (Sigma) or anti-CD3 (eBioscience) was used at 5 μg/ml as a positive control. Plates were then incubated for 12 h at 4 °C with rat anti-mouse biotin-conjugated IFNγ (BD PharMingen), followed by 3 h at 25°C with streptavidin-AKP (BD PharMingen) and finally with NBT/BCIP (Pierce) for color development. An ELISPOT reader (AID, Germany) was used to count the spots.

Chromium release assay

Target cells were radioactively labeled by 1h incubation with hexavalent chromium-51 (Beckman Coulter). MBL-2 cells were pulsed with hTERT or OVA peptide as positive and negative controls. OVA-specific or mTERT cells were prepared as indicated above. T cells and target cells were mixed at different ratios and incubated for 5h at 37°C. Subsequently, the supernatants were collected and placed for registration in Luma Plates (Perkin Elmer). Gamma radiation emission was measured as ''counts per minute'' (cpm) for each well with a TopCount NXT™ Microplate Scintillation and Luminescence Counter (Perkin Elmer). To measure maximum cpt level (cpm^{max}) cells were lysed by addition of 1% Triton X-100 in water. Culture medium alone was used as negative control to quantify spontaneous radiation emission (cpm^{spont}). Specific lysis in experimental wells was calculated with the formula:

$$\%\ lysis = \frac{cpm^{exp} - cpm^{spont}}{cpm^{max} - cpm^{spont}} \times 100\%$$

Adhesion assay with spheroids

Spheroid formation was performed in 6-well plates. Agar Noble 4% was pre-warmed and mixed with normal DANG culture RPMI medium in 1:1 ratio and 1 ml was layered on one the plate well and solidified. DANG and DANG-CLDN18 cells were plated on top of the agar in normal RPMI culture medium for 3 days or longer until average spheroid diameter reached 210 μm. Single spheroids were size-selected and picked under a microscope and transferred on agar-layered 24 well-plate, 10 spheroids per well. hTERT-specific T cells were pre-stained with CellTrace (Thermo Fisher Scientific MA - USA) and $1x10^6$ cells were seeded on top of the agar and cultured for 4h. Afterward, the spheroids were extensively washed in PBS to remove the unattached T cells and were plated in complete white RPMI in chamber slides with matrigel. Spheroids were counterstained with DAPI and chamber slides were imaged with a Leica TCS SP5 AOBS confocal-multiphoton system. To enumerate T lymphocytes attached to spheroids, ten spheroids were pooled in the same well and GFP quantified by IVIS spectrum Imaging System (Perkin Elmer, Waltham, MA, USA).

T cell migration assay

DANG and DANG-CLDN18 cells were plated in T75 flasks and conditioned media was collected 72 hours later when cell confluence achieved 80%. CFSE labeled hTERT-specific T cells were seeded on 5 μm-pore transwells (Corning, NY - USA) placed in wells with cancer cell supernatants. CD3-CD28 stimulated T cell conditioned medium was used as a positive control, whereas complete RPMI was used as a negative control. T cells were allowed to migrate for 5h then cells were detached with PBS containing 0.2% EDTA and migrated cells were counted with BD Trucount™ Absolute Counting Tubes (BD, NJ, USA).

Competition immunological synapse formation

$CLDN18^{+/+}$ clones were stained with Cell trace. Different FC1199-OVA $CLDN18^{+/+}$ and $CLDN18^{-/-}$ cell clones were mixed each other in a 1:1 ratio. OVA-specific CTLs and target cells were mixed 1:1 with tumor cells and immediately plated on polylysine-coated coverslips in a 24-well plate. Cells were incubated for 1h at 37°C and then fixed in 4% PFA for 15 min at RT, before immunofluorescence staining. Fixed cells were permeabilized in Triton-X-100 0.1% in PBS for 30 min at RT, blocked for 2h at RT in 20% normal goat serum in permeabilization solution, then incubated overnight at 4°C with BV421-conjugated antibody anti-mCD3 diluted in PBS. Samples were washed with Tween-20 0.05% in PBS before confocal microscopy acquisition.

Immunological synapse was identified as the site of CD3 accumulation on T cells at the contact site with cancer cells. The number of immunological synapses (Nsyn) was counted in each sample for $CLDN18^{+/+}$ cells and $CLDN18^{-/-}$ cells, and normalized to the total number of $CLDN18^{+/+}$ cells and $CLDN18^{-/-}$ cells respectively (Ntot). Nine fields were analyzed for each sample. That is described by formulae:

$$\%\ CLDN18^{+/+}\ Cancer\ cells\ forming\ synapses = \frac{Nsyn\ CLDN18^{+/+}}{Ntot\ CLDN18^{+/+}};$$

$$\%\ CLDN18^{-/-}\ Cancer\ cells\ forming\ synapses = \frac{Nsyn\ CLDN18^{-/-}}{Ntot\ CLDN18^{-/-}}.$$

Molecular analysis

Gene expression analysis on microarray and bulk RNA-seq data

For microarray analysis, we prepared n = 3 biological replicates of FC1199-OVA and n = 3 FC1242-OVA lines. Total RNA was extracted using RNeasy Mini Kit (Qiagen, Hilden, Germany), and contaminant DNA was removed by RNase-Free DNase Set (Qiagen, Hilden, Germany). RNA quality and purity were assessed on the Agilent Bioanalyzer 2100 (Agilent Technologies, Milano, Italy); RNA concentration was determined using the NanoDrop ND-1000 Spectrophotometer (NanoDrop Technologies). Labeling and hybridization were performed according to Affymetrix One Cycle Target Labeling protocol on HG-U133 Plus 2.0 arrays (Affymetrix, Thermo Fisher Scientific, Waltham, MA, USA). Microarray data are available at Gene Expression Omnibus under accession GSE230868. The analysis of microarray and bulk RNA-seq data was performed with the R/Bioconductor platform. The raw probe level signals of the microarray were processed for background correction, normalization and summarization using the robust multi-chip average algorithm (RMA).[65–67] Differential gene expression analysis between FC1199-OVA and FC1242-OVA lines was performed using limma package.[68] Only the genes with an adjusted p-value < 0.05 were considered statistically significant. Probes with ambiguous differential behavior were removed from the downstream analyses. Pathway analysis was performed using DAVID web application[69] on the Gene Ontology (GO FAT) categories using the following procedure. (1) A first enrichment analysis was performed using both up- and downregulated genes in the comparison between FC1199-OVA vs FC1242-OVA to retrieve the regulated biological processes (BP) and cellular components (CC). A separate analysis was performed with only up- (2) or down-regulated (3) genes. (4) For each list of enriched processes, only the categories obtained also in (1) were retained. (5) The list of categories obtained in (2) and (3) were further filtered removing those categories present in both lists and having a smaller number of enriched genes compared to the other. In all the previous steps only the GO categories with an FDR < 0.05 were considered statistically significant. Scores on gene sets both for the microarray and bulk RNA-seq data were calculated using gene set variation analysis (GSVA).[27] The expression of *CLDN18* was analyzed on the PAAD, LUAD and LUSC TCGA datasets[32] annotated with PDAC[15–17] and NSCLC molecular subtypes.[33] Statistical comparisons were performed using Kruskal-Wallis followed by Dunn's test considering p < 0.05 statistically significant. The TCGA datasets were obtained from the R package 'curatedTCGAData'[70] selecting the normalized RSEM gene expression assays. Associations between *CLDN18* expression and 'EMT', 'Signaling by MET', 'Hippo signaling pathway', 'HIF-1 signaling pathway', 'Antigen processing', 'Adherens junction' and 'Cell-cell communication' in the ICGC dataset[17] were estimated using linear regression models. The Spearman correlation between *CLDN18* and *CD3E* expression was performed using the R package 'ggpubr' (https://CRAN.R-project.org/package=ggpubr). Gene signatures of RNA-seq data on T cells low and T cell high sorted tumor samples[25] were obtained performing differential expression analysis using DESeq2 R package[74] and selecting upregulated genes with an adjusted p-value < 0.05 in each condition. GSVA scores on FC1199-OVA and FC1242-OVA cell lines and T cells^{lo} and T cell^{hi} sorted tumor samples on Bailey's PDAC molecular classifications[17] were compared using t-test. The mapping between mouse and human gene symbols was performed using the R package biomaRt.[75]

Survival analysis

Survival analyses were performed using Kaplan-Meier curves. Cut points for stratifying patients were estimated using the maximally selected rank statistics implemented in the R package 'maxstat' (https://CRAN.R-project.org/package=maxstat). The R packages 'survminer' (https://CRAN.R-project.org/package=survminer) and 'RTCGA' (https://rtcga.github.io/RTCGA) were also used for the survival analyses. The comparison of survival curves was performed using logrank p-values considering statistically significant only comparisons with a p-value < 0.05. Cox regression models were fitted adjusting the effect of CLDN18 and TILs for the following covariates: age, gender, residual tumor, and stage. Martingale residuals were used to assess the functional form of the continuous covariates and to assess the overall fit of the Cox model. Nonlinearity of the parameter "age" in the tissue microarray and PDAC ICGC[17] datasets was addressed using spline terms. The proportional hazards assumption was checked using the Schoenfeld residual-based test. The variable "stage" was stratified in the model for the PDAC ICGC[17] and TCGA LUAD[33] datasets because it violated the proportional hazard assumption. Multicollinearity was checked computing the variance inflation factors (VIF). The significance of the parameters was assessed through the analysis of variance (ANOVA) considering a p-value < 0.05 statistically significant. Hazard ratios (HR) for continuous parameters were computed as interquartile range (IQR) effects. The statistical analysis was performed with the R packages 'rms' (https://CRAN.R-project.org/package=rms) (v6.5-0) and 'survival' (https://CRAN.R-project.org/package=survival) (v3.2-11).

Real time-PCR

Total RNA from FC1199-OVA and FC1242-OVA tumors was isolated from immunocompromised mice that did or did not receive ACT. Samples were preserved in RNAlater solution (Thermo Fisher Scientific MA - USA) and kept on ice. Before the RNA extraction procedure, the RNAlater solution was removed and tripleXtractor (Grisp) was added. The tumor pieces were homogenized (GentleMacs-Miltenyi Biotec) and incubated for 5 minutes at room temperature. Total RNA was extracted by chloroform and its amount and purity was analyzed by the ND-1000 Spectrophotometer (NanoDrop Technologies). cDNA was generated from 1 ug RNA using RevertAid RT Reverse Transcription Kit (Thermo Fisher Scientific MA - USA) according to the manufacturer's instruction. Semiquantitative real-time PCR was run using SYBR® Green PCR Master Mix (Thermo Fisher Scientific MA - USA). All samples were normalized to *Gapdh* housekeeping gene. Post-qRT-PCR analysis to quantify relative gene expression was performed by the comparative Ct method ($2^{-\Delta\Delta Ct}$).

Flow cytometry

For the extracellular staining 1x10^6 cells were blocked with Fc blocking anti-mouse CD16/32 prior to staining (Biolegend) or anti-human (Miltenyi Biotec) for 10 minutes at RT. The following anti-mouse mAbs were then used for 30 min at 4 °C: CD11b (M1/70), CD45 (30F-11), CD3 (17A2), CD8a (53-6.7), TCR Vß5.1,5.2 (MR9-4), MHC-I (SF1-1.1), ICAM-1 (YN1/1.7.4), ALCAM (eBioALC48), E-cadherin (DECMA-1), CD62P (Psel.K02.3), VCAM-1 (429 MVCAM.A), PSGL-1 (4RA10), CLDN18 (Imab 362 kindly provided by Ö. Türeci and U. Sahin), LIVE/DEAD dyes (ThermoFisher Scientific). For human cells we used the following anti-human hCD3 (SK7; Cat#557832). All the antibodies were purchased from the following companies: BD Bioscience (San Jose, CA, USA), eBiosciences (ThermoFisher Scientific, Waltham, MA, USA), Bio-rad Laboratories (Hercules, CA, USA) and Biolegend (San Diego, CA, USA). For the intracellular staining 1x10^6 cells were fixed with eBioscience™ Foxp3 / Transcription Factor Fixation/Permeabilization Concentrate and Diluent (ThermoFisher Scientific) and permeabilized with Permeabilization Buffer ((ThermoFisher Scientific) according to the product datasheet. The following Ab was then used for 30 min at RT in permeabilization buffer after FcR blocking reagents for 15 min at RT: CLDN18 polyclonal antibody (ThermoFisher Scientific). Samples were acquired with FACS Canto II (BD, Franklin Lakes, NJ, USA) and analyzed by FlowJo software (Tree Star, Inc., Ashland, OR, USA).

Proteomic studies

Western-blot and quantification

Whole cell lysates of FC1199, FC1199-OVA, FC1242 and FC1242-OVA cells were generated in 200 µl TRITON buffer containing 0.5% Triton X-100, 50 mM Hepes, 150 mM NaCl, 5 mM EDTA, 1 mM NaOV4, 2 mM PMSF, and protease inhibitors. Samples were incubated on ice for 15 minutes then subjected to BCA protein quantification (ThermoFisher Scientific).

Samples were prepared in Laemmli Buffer supplemented with 10% β-mercaptoethanol and denatured at 97°C for 7 min. Insoluble materials were removed by centrifugation. Samples were subjected to SDS polyacrylamide 10% Tris-Glycine or Bis- Tris gel electrophoresis and blotted onto PVDF-membranes (Immobilon P membranes, Millipore, Billerica, MA, USA). Tris-buffered saline plus 0.05% Tween-20 and 5% non-fat dry milk were used to block unspecific sites. The following primary and secondary antibodies were used: ovalbumin polyclonal antibody (ThermoFisher Scientific), rabbit HRP-conjugated anti-GAPDH (Cell Signalling Technologies, Danvers, MA, USA), mouse monoclonal anti 6x-His Tag (clone HIS.H8), goat polyclonal anti-CD166, rabbit polyclonal anti-Caveolin 1, rabbit monoclonal anti-Telomerase reverse transcriptase (clone Y182) and mouse HRP conjugate anti β-Actin (clone 8H10D10). Proteins were revealed by GE ImageQuant LAS400 with standard or Femto substrate (ThermoFisher Scientific). Western-blot was quantified by ImageJ software through Analyze>Gels>Label Peaks function and normalized on actin/GAPDH loading controls.

ELISA

Multiplex or single cytokine (IL-3, CXCL10, CCL5, IFN-γ) ELISA (Thermo Fisher Scientific, MA, USA) were performed on supernatants from OVA-specific T cells co-cultured with cancer cells at ratios of 0.5:1, 1:1, 2:1 and 4:1 for 24 hours. In some experiments the co-culture was performed in presence of CD6 blocking antibody or isotype control. Supernatant from T cells cultured alone was used as negative control and the value subtracted from the experimental samples.

Lipid raft isolation by sucrose gradient centrifugation, characterization and analyses

Lipid rafts were isolated using previously described methods,[43] employing the detergent 1% Brij58 in TNEV buffer (Hris-HCl, NaCl, EDTA, Na_3VO_4) and sucrose-gradient centrifugation. Cells were scraped in ice cold PBS, counted and lysed with detergent treatment (supplemented with PMSF, protease and phosphatase inhibitor cocktail) 1 hat 4°C and then homogenized with Potter-Elvehjem. In order to remove unbroken cells, nuclei and cellular debris the homogenate was centrifuged and the supernatant was fractionated in sucrose gradient (42.5%, 35%, 5%) and centrifuged in a SW41 Ti (Beckman Coulter) at 39000 rpm for 19 h at 4°C. A total of ten 1-ml fractions were collected from the top of the gradient to the end of the tube. Fractions were kept frozen at -20°C until use. Lipid rafts were located at fractions 3-4. The concentration of proteins, cholesterol and phospholipids in each fraction was measured by a BCA protein assay kit, a cholesterol assay kit and a phospholipids B kit. Immunoblot analysis was used for specific protein detection: 30 µl of each fraction was diluted with sample buffer, run on NuPAGE™ 10%, Bis-Tris, 1.0 mm, Midi Protein Gels and transferred onto PVDF membranes. Membranes were sequentially incubated with primary antibodies overnight at 4°C and the day after with horseradish peroxidase-conjugated secondary antibodies. Bound antibody complexes were detected by ECL.

Immunoprecipitation

FC1242-CLDN18-His and FC1242 cells were solubilized in extraction RIPA buffer and then subjected to BCA protein quantification for the immunoprecipitation of CLDN18.

Clarified cell lysates were incubated with an anti-His antibody or an IgG mouse antibody with rotation and incubation O.N. at 4°C. Then the samples were recovered with DynabeadsTM Protein G (ThermoFisher Scientific) and bound to the magnetic beads during a short incubation with rotation. The resulting antibody complexes with beads were washed 3 times with PBS prior to immunoblot analysis.

Live Imaging

Live cell imaging of in vitro co-cultures and analysis

OVA-specific CTLs cells were co-cultured on the day of imaging with FC1199-OVA CLDN18$^{+/+}$ and CLDN18$^{-/-}$ cells at a 1:1 ratio. Lymphocytes were allowed to seed for 30 minutes and then activation and dynamics of CTL motility and the susceptibility of PDAC clones to CD8$^+$ T cell-mediated cytotoxicity were measured. For T cell activation analysis BioTracker 609 Red Ca2$^+$ AM

dye (Merck-Millipore) was used to label OVA-specific CTLs. T cells alone were used as control. For the study of the $CD8^+$ T cell dynamics after co-culture with PDAC cells, lymphocytes were labelled with PKH26 red (Merck-Millipore) and their motility behavior was measured every minute for one hour. For the study of the $CD8^+$ T cell dynamics after ALCAM blockade, PDAC cells were treated for 30 min before imaging with a solution of 50 μg/ml (V_{fin} 200 μl) of anti-ALCAM antibody (I/F8-Fc bivalent Fc fusion protein) or isotype control (KSF-Fc bivalent Fc fusion protein). Similarly, $CD8^+$ T cell dynamics with $CLDN18^{+/+}$ and $CLDN18^{-/-}$ PDAC cells were tracked in presence of anti-ALCAM antibody (I/F8-Fc bivalent Fc fusion protein) or monoclonal anti-CD6 antibody (Clone 96117, R&D) or isotype controls (KSF-Fc bivalent Fc fusion protein, clone HRPN BioXcell, for ALCAM and CD6 respectively). In addition, to determine $CD8^+$ T cells-induced cytotoxicity, PDAC cells were monitored every 30 minutes for six hours. PDAC cells alone were used as control. For all live imaging experiments, cells were resuspended in phenol-red free medium. Images were acquired with a 40x Plan apochromatic objective (NA 0.6) mounted on an Axio Observer.Z1/7 inverted wide-field microscope (Carl Zeiss Microscopy) equipped with a thermostatic chamber. The environmental conditions were kept at 37°C in the presence of 5% CO_2. Exposure time for bright field and fluorescence channels was automatically set and left unchanged for the entire duration of the experiment. The multi-field acquisition was achieved using the Tiles tool of Zen v3.5 software (Carl Zeiss Microscopy). The focus plane for each region of interest was automatically set at every time point using the Autofocus tool of Zen v3.5 software (Carl Zeiss Microscopy). For the analysis of T cell motility, individual image acquisitions were converted to movie format and analyzed using Imaris software (Bitplane). Cell tracks were automatically computed using the Spot tool of Imaris software. Only $CD8^+$ T cells in contact with PDAC cells were considered for the analysis. The following motility parameters were calculated: mean velocity (μm/s) displayed by each cell along its path, the arrest coefficient (determined as the proportion of time in which the cell is not moving) and the duration of stable contacts (min) between the OVA-specific CTLs and the FC1199-OVA $CLDN18^{+/+}$ and $CLDN18^{-/-}$ cells. The susceptibility of tumor cells to OVA-specific CTL-induced cytotoxicity was assessed with the Confluency BioApp of Zen v3.5 software (Carl Zeiss Microscopy), by measuring the reduction over time of the area (μm^2) covered by PDAC cells. Particularly, the GFP^+ area was automatically calculated for every time point of each movie and the values of area computed for each time point were normalized on the area covered by PDAC cells at the initial time point, defined as T0. Accordingly, data were expressed and plotted as the percentage of GFP^+ area compared to T0 over time.

Intravital tumor imaging preparation

OVA-specific CTLs were labeled for 45 min at 37°C with 40 mM 7-amino-4-chloromethylcoumarin (CMAC) (Invitrogen - ThermoFisher Scientific) and 2×10^7 of CTLs were transferred by i.v. injection into immunocompromised $Rag2^{-/-}$ (B10;B6-*Rag2*^{tm1Fwa} *Il2rg*^{tm1Wjl}) mice bearing FC1199-OVA $CLDN18^{+/+}$ and $CLDN18^{-/-}$ tumor cells when the tumor reach 10 mm x 10 mm of volume. Forty-eight hours later, mice were anesthetized by intraperitoneal (i.p.) injection of ketamine (100 mg/kg body weight)/xylazine (15 mg/kg) solution and prepared for the surgery. Hair on the back was shaved, skin was sterilized with 70% ethanol and an incision was made to expose the tumor mass. The anesthetized mouse was fitted on a customized microscope stage after microsurgery, minimizing respiratory-induced movements.

Two-photon imaging acquisition and data analysis

Imaging was performed on a customized upright Leica TCS SP5 AOBS confocal-multiphoton system using a thermostatic blanket system to maintain mouse temperature at 37°C. CMAC- labeled OVA-specific CTLs and GFP^+ tumor cells were excited with a mode-locked Ti:Sapphire Chameleon Ultra II laser (Coherent Inc) and visualized with an Olympus XLUMPlanFI 20x/0.95 water immersion objective. Fluorescence emission from the two different fluorescent dyes was separated through panchromatic electronic barrier filters and detected as green (490–560 nm), and blue (400-500 nm) signal. Stacks of images were acquired using the Leica acquisition software, by scanning volumes of tissue, typically 75-100 μm of z-stacks and sampling every 2 μm. To create time-lapse sequences, image stacks were acquired at 30 s time intervals for 30-60 min movies. Multidimensional rendering was performed with Imaris (Bitplane). Raw image files were imported into the Imaris software (Bitplane) to be transformed into volume-rendered three-dimensional movies, and cell movement analysis was performed. The three-dimensional spatial position of each cell was detected based on centroid fluorescence intensity. Tracking and segmentation of lymphocytes were performed with Imaris Spots function in which tracks from each cell consisting of serial sets of xyz coordinates of single cell centroid. Once the cell tracks have been created on a robust number of cells several parameters can be used to describe the migration dynamics of cells quantitatively as described in Dusi et al.[76] and Zenaro et al.[77]

Histopathology analysis and digital image analysis

After mice were euthanized, tumor samples and organs were resected and fixed in 10% neutral buffered formalin overnight. Samples were embedded into paraffin. For immunohistochemistry of paraffin-embedded samples, 3 μm thick tissue sections were cut using a microtome (Leica), samples were deparaffinized and rehydrated. Following antigen retrieval procedure, primary antibodies were added for overnight incubation at 4 °C. MID (Thermo Fisher Scientific/Invitrogen) was used for CLDN18 staining at concentration 0.2 μg/ml overnight (alternative: 1.5 μg/ml, 1h, at room temperature). Abcam anti-CD3 antibody (ab16669), clone SP7 was used for lymphocyte staining at working dilution 1:500, 1h, at room temperature or overnight staining at 4°C. Secondary antibodies were incubated for 30 minutes at room temperature (Power-Vision HRP anti-Rabbit for CLDN18 & CD3 staining). Immunoreactive antigens were detected using streptavidin peroxidase Vector NovaRED (Vector Laboratories) for CD3 staining and Permanent HRP Green (Zytomed) for CLDN18 staining. After chromogen incubation, slides were counterstained in Hematoxylin (Thermo Fisher Scientific) and brightfield images were scanned with a Whole Slide Scanner (Axio Scan.Z1 (Carl Zeiss Microscopy) & NanoZoomer S360 (Hamamatsu Photonics). Digital Image Analysis and cell quantifications were done with Tissue Studio (Definiens) and HALO

software (Indica Labs). For the first xenograft models FC1199, FC1242 and DANG, CLDN18 expression (CLDN18$^+$ tumor tissue area), CD3 count, and localization was detected by Tissue Studio (Definiens) and visualized in a Heatmap illustration. As follow up DANG-CLDN18 analysis on 11 new xenografts was performed with HALO software (adapted algorithm: Immune Cell v1.3) to separate Tumor tissue, Necrosis, and capsule using an inbuild classifier. For the cell-based analysis of Claudin 18 expression, CD3 count, and localization were determined and visualized in a tumor core analysis based on the mid of each tumor (500 μm bins). For the human PDAC cohort study, 148 cases in 8 TMA slides were double stained for CD3 lymphocytes and CLDN18 expression. For each CLDN18$^+$ TMA-Spot the localization of CD3$^+$ lymphocyte was defined. The distance between CD3$^+$ immune cells and their next CLDN18$^+$ tumor cell was measured. The distance range was split in 11 bins (10x bins for 0-100 μm and 1 bin 100 μm < X). For the CLDN18$^+$ spots the Immune Cell Distance was detected. The analysis was performed using the HALO and Spotfire software suite. For the murine KP lung adenocarcinoma model, lungs were freshly isolated, and tumor burden was evaluated by bioluminescence imaging 18 weeks following virus instillation. A veterinary pathologist blindly defined the number of lesions, size and grade of each lesion/lung layer in a three-tier grading system (grade 1, G1, well differentiated, low grade; grade 2, G2, moderately differentiated, intermediate grade; grade 3, G3, undifferentiated, high grade) according to DuPage et al.[38] and Nikitin et al.[39] Tumor classification by grading (G1, G2, G3) was performed on the hematoxylin Eosin of the staged mouse lungs and plotted in HALO Link. The annotations were transferred into the HALO software and analyzed (adapted algorithm: HighPlex FL v4.1.3).

Immunofluorescence and digital image analysis

Tumor samples were fixed in 10% neutral buffered formalin and embedded into paraffin. For immunofluorescence of paraffin-embedded samples, 3 μm thick tissue sections were cut using a microtome, deparaffinized and rehydrated semi-automatically using the Ventana Discovery XT Stainer (Roche). Following antigen retrieval procedure, primary antibodies were added consecutively for 60 min at 37 °C.

On human pancreatic tumor tissue Ganymed anti-CLDN18 antibody, clone 43-14A at a concentration of 0.25 μg/ml was used for CLDN18 staining. Roche Ventana anti-CD4 antibody, clone SP35 (ready to use), anti-CD3 antibody, clone 2GV6 (ready to use) and Novus Biologicals, clone SP16 (1:100), were used for lymphocyte staining. Secondary antibodies were incubated for 32 minutes at 37°C (OmniMap anti-Rabbit HRP for CD4, CD8 and CD3 staining and OmniMap anti-Mouse HRP for Claudin 18 staining (Roche Ventana). Immunoreactive antigens were detected using Opal Fluorophore (Akoya Biosciences). CD4 – Opal 520, CD8 – Opal 570, CD3 – Opal 620, CLDN18 – Opal 690. On murine lung adenocarcinoma model Thermo Fisher Scientific anti-CLDN18 antibody, clone 34H14L15 (Cat. 700178) at a concentration of 0.1 μg/ml was used for CLDN18 staining. Sino Biological anti-CD4 antibody, clone 766 (1:200) and Thermo Fisher Scientific anti-CD8a antibody, clone 4SM15 at concentration 5 μg/ml were used for lymphocyte staining. Secondary antibodies were incubated for 32 minutes at 37°C (OmniMap anti-Rabbit HRP for CD4 and Claudin 18 staining and OmniMap anti-Rat HRP for CD8a staining (Roche Ventana). Immunoreactive antigens were detected using Opal Fluorophore (Akoya Biosciences). CD4 – Opal 520, CD8a – Opal 570, Claudin 18 – Opal 690. After fluorophore incubation (20 min) slides were counterstained with DAPI (Sigma Aldrich).

Immunofluorescence images were scanned with a Whole Slide Scanner (PhenoImager (Akoya Bioscience). Digital Image Analysis and cell quantification was performed with the HALO (Indica Labs). 11 IF-stained human pancreatic PDAC tumor samples were analyzed with HALO software (adapted HighPlex algorithm). To perform tumor classification, pathologist expertise was employed to draw the classes: Invasive tumor, PanIN 1, PanIN 2, PanIN 3, and normal endocrine pancreas, using HALO Link (Indica Labs). Cell analysis for CLDN18, CD3, CD4, CD8 was performed within the respective annotations to collect values for each tumor stage to subsequently display number and distribution in the density heatmap as phenotypes within 250 μm.

Cell line immunofluorescence and image acquisition

FC1199-OVA CLDN18$^{+/+}$ or FC1199-OVA CLDN18$^{-/-}$ cells were grown in chamber slides (Lab-Tek-II- Thermo Fisher Scientific) and fixed with PFA 4% for 10 min prior to blocking of unspecific binding sites with PBS-BSA 1%. for 2 hours at RT. in Staining was done with a polyclonal unconjugated anti-ALCAM antibody at 1:400 (Thermo Fisher Scientific) overnight at 4°C in PBS-BSA1%. Then, secondary antibody donkey anti-goat AF546 IgG (Thermo Fisher Scientific) 1:500 in PBS + 1% BSA was added for 1 hour at RT and GFP was visualized as a cell co-stain. For colocalization studies of CLDN18 and adhesion molecules FC1199 cells were grown in chamber slide as described above and staining was performed with the primary antibodies anti-CLDN18 (Imab 362) 1:500, anti-ALCAM (Thermo Fisher Scientific) 1:400, anti-ICAM-1 (Biolegend) 1:100 in PBS-BSA 1% O/N at 4°C. Then, a donkey anti-goat AF680 IgG (Thermo Fisher Scientific), a goat anti-human AF405 IgG (Thermo Fisher Scientific) both 1:500 or a goat anti-rat AF405 IgG (Thermo Fisher Scientific) 1:250 in PBS-1% BSA were added for 1 hour each at RT. Gold Prolong Antifade (Thermo Fisher Scientific) was used to mount coverslips (Menzel-Gläser) prior to the visualization of slides.

For ALCAM cell surface expression images were captured on an Axio Imager Z2 microscope (Carl Zeiss Microscopy). Images were acquired with a constant exposure time determined by staining with secondary antibodies alone. Acquired images were quantified on 6 ROI per field, blindly choosen on the GFP channel. Nine fields were acquired for each cell clone and the fluorescence of the ALCAM adhesion molecule was measured by ImageJ using the same threshold. Results were then represented as median fluorescent ALCAM expression normalized to mm^2. For colocalization study images were captured on a Leica TCS SP5 AOBS confocal equipped with a Plan-Apochromat 63x oil immersion objective. Excitation lasers used were 405nm and 633 nm and detectors were set according to the corresponding fluorophores used. Typically, images were acquired at 512 x 512 pixels, 400 Hz scan speed and with the pinhole set to 0.95 Airy unit. At least nine fields were acquired for each well chamber. Raw image files were imported into the Imaris software (Bitplane). A colocalization channel of CLDN18, ALCAM or ICAM-1 on cell surface membrane of the FC1199 cell line was

made in Imaris using the Colocalization tool. Surface function was used to segment protein expression and masked them onto separate channels before applying colocalization to avoid background signal.

QUANTIFICATION AND STATISTICAL ANALYSIS

All statistical analyses were carried out using GraphPad Prism software. Comparisons between two groups were performed, unless otherwise indicated, using either a two-tailed unpaired Student's t-test or Mann-Whitney test, depending on the normality of distribution. For *in vivo* experiments, the expected heterogeneity of the samples, the significance threshold, the expected or observed difference, and previous publications were taken into consideration while determining the sample size. Unless otherwise indicated, all experiments show data as mean with all data points or group mean ± SD or mean ± SEM. Two-way ANOVA tests were used to compare tumor growth, with Bonferroni's multiple comparison follow-up test. Statistics are all included in figures, with a P value less or equal to 0.05 defined as significant.